The Astrophysical Journal, 1011:87 (16pp), 2026 November 1 https://doi.org/10.3847/1538-4357/aeac53
© 2026. The Author(s). Published by the American Astronomical Society.
OPEN ACCESS

Metal-poor Brown Dwarf Kinematics from JWST NIRSpec Spectroscopy

Chih-Chun Hsu[1], Christopher A. Theissen[2], Adam J. Burgasser[2], Adam C. Schneider[3], Christian Aganze[4], Aaron M. Meisner[5,6,7], Jonathan Gagné[8,9], Nicolas Lodieu[10,11], ZengHua Zhang[12,13], Genaro Suárez[14], Eileen C. Gonzales[15], Jacqueline K. Faherty[14], Jason J. Wang (王劲飞)[1,16], Stanimir A. Metchev[17], Dan Caselden[14], Michael C. Cushing[18], and Roman Gerasimov[19]

[1] Center for Interdisciplinary Exploration and Research in Astrophysics (CIERA), Northwestern University, 1800 Sherman Ave., Evanston, IL 60201, USA; chsu@northwestern.edu
[2] Department of Astronomy & Astrophysics, University of California San Diego, La Jolla, CA 92093, USA
[3] United States Naval Observatory, Flagstaff Station, 10391, West Naval Observatory Rd., Flagstaff, AZ 86005, USA
[4] Department of Physics, Stanford University, Stanford, CA 94305, USA
[5] NSF National Optical-Infrared Astronomy Research Laboratory, 950 N. Cherry Ave., Tucson, AZ 85719, USA
[6] Center for Astrophysics | Harvard & Smithsonian, 60 Garden St., Cambridge, MA 02138, USA
[7] Radcliffe Institute for Advanced Study at Harvard University, 10 Garden St., Cambridge, MA 02138, USA
[8] Planétarium de Montréal, Espace pour la Vie, 4801 Ave. Pierre-de Coubertin, Montréal, Québec, Canada
[9] Trottier Institute for Research on Exoplanets, Université de Montréal, Département de Physique, C.P. 6128 Succ. Centre-ville, Montréal, QC H3C 3J7, Canada
[10] Instituto de Astrofísica de Canarias (IAC), Calle Vía Láctea s/n, E-38200 La Laguna, Tenerife, Spain
[11] Departamento de Astrofísica, Universidad de La Laguna (ULL), E-38206 La Laguna, Tenerife, Spain
[12] School of Astronomy and Space Science, Nanjing University, 163 Xianlin Ave., Nanjing 210023, People's Republic of China
[13] Key Laboratory of Modern Astronomy and Astrophysics, Nanjing University, Ministry of Education, Nanjing 210023, People's Republic of China
[14] Department of Astrophysics, American Museum of Natural History, Central Park West at 79th St., New York, NY 10024, USA
[15] Department of Physics and Astronomy, San Francisco State University, 1600 Holloway Ave., San Francisco, CA 94132, USA
[16] Department of Physics and Astronomy, Northwestern University, 2145 Sheridan Rd., Evanston, IL 60208, USA
[17] Department of Physics and Astronomy, The University of Western Ontario, 1151 Richmond St, London, ON N6A 3K7, Canada
[18] Ritter Astrophysical Research Center, Department of Physics & Astronomy, University of Toledo, 2801 W. Bancroft St., Toledo, OH 43606, USA
[19] Department of Physics and Astronomy, University of Notre Dame, Nieuwland Science Hall, Notre Dame, 46556, IN, USA
Received 2026 August 7; revised 2026 September 23; accepted 2026 September 23; published 2026 October 28

Abstract

Galactic archaeology relies on stellar kinematics and chemical abundances to identify various stellar populations and associations. With JWST, Galactic archaeology of ancient metal-poor brown dwarfs is now possible through high-sensitivity, medium-resolution spectroscopy. We present the first metal-poor brown dwarf radial velocity (RV) survey using JWST/NIRSpec G395H spectra ($\lambda/\Delta\lambda \sim 3000$) for a sample of 23 LTY dwarfs across a wide range of temperatures and metallicities. We introduce a forward-modeling framework to measure robust RVs for brown dwarfs by focusing on the CO fundamental band at $\sim$4.5 μm. By comparing to sources with existing high-resolution RV measurements, we demonstrate that G395H RVs can achieve a systematic uncertainty of 5 km s^{-1}, sufficient to examine their Galactic space motions. We identify kinematic members of the Milky Way's thin disk, thick disk, and halo populations in this sample. We also confirm WISE J155349.98+693355.2 as likely associated with the Gaia–Enceladus merger remnant, and 2MASS J05325346+8246465 is likely associated with the Thamnos stream. Our study systematically demonstrates that JWST G395H spectroscopy can provide robust RVs in addition to detailed chemical abundances, necessary for Galactic archaeology studies. Future discoveries and characterization of brown dwarfs associated with Galactic halo substructures and streams will enable a stringent test of stellar/substellar formation and evolutionary models for diverse metallicities.

Unified Astronomy Thesaurus concepts: Brown dwarfs (185); Stellar kinematics (1608); Stellar populations (1622); L subdwarfs (896); T dwarfs (1679); T subdwarfs (1680); Y dwarfs (1827)

Materials only available in the online version of record: figure set

1. Introduction

Galactic archeology is the study of various stellar populations in the Milky Way, combining kinematic and chemical information. Thanks to major surveys such as the Sloan Digital Sky Survey (SDSS; K. N. Abazajian et al. 2009), Gaia (Gaia Collaboration et al. 2016), GALAH (G. M. De Silva et al. 2015), APOGEE (S. R. Majewski et al. 2017), H3 (C. Conroy et al. 2019), DESI (A. P. Cooper et al. 2023), major findings include the discoveries of in situ and accreted halo components (P. E. Nissen & W. J. Schuster 2010), the Gaia-Enceladus dwarf galaxy merger remnant (V. Belokurov et al. 2018; A. Helmi et al. 2018; G. C. Myeong et al. 2018; P. Di Matteo et al. 2019; C. Gallart et al. 2019), dozens of stellar streams (A. Helmi 2020; A. Bonaca & A. M. Price-Whelan 2025), among others (see e.g., A. J. Deason & V. Belokurov 2024 for a recent review). These findings allow us to study the Milky Way's assembly history and mass distribution, as well as constrain dark matter distribution in the Milky Way's gravitational potential (A. Helmi 2008; Ž. Ivezić et al. 2012; V. Belokurov 2013; H.-W. Rix & J. Bovy 2013; J. Bland-Hawthorn & O. Gerhard 2016; S. Chakrabarti et al. 2022).

Galactic archeology has largely focused on main-sequence and giant stars as tracer populations. However, at the lowest masses, brown dwarfs provide an alternate population to study the

Original content from this work may be used under the terms of the Creative Commons Attribution 4.0 licence. Any further distribution of this work must maintain attribution to the author(s) and the title of the work, journal citation and DOI.

evolution of the Milky Way system. These objects are thought to form similarly to stars but have insufficient mass to sustain hydrogen fusion ($M \lesssim 0.075\ M_{\odot}$; S. S. Kumar 1962, 1963; C. Hayashi & T. Nakano 1963). Discovered just over three decades ago (T. Nakajima et al. 1995; R. Rebolo et al. 1996), we now know that brown dwarfs are ubiquitous in our Milky Way, but are more difficult to uncover and characterize than their brighter stellar counterparts (J. D. Kirkpatrick 2005). Studying substellar populations in the Milky Way through their kinematics and chemical composition enables a new means to study the Galaxy's formation and evolution history. These substellar populations have essentially infinite lifetimes, and their relative abundances compared to lowest-mass stellar populations enable direct measurements of stellar/substellar mass function, birth rates, and chemical evolution (J. D. Kirkpatrick 2005). These populations do not fuse species including hydrogen and lithium ($\lesssim$0.060 $M_{\odot}$; A. Burrows et al. 2001) and are fully convective such that they preserve their initial chemical compositions, offering a unique and important probe into cosmic chemical evolution since the birth of the Milky Way.

Previous 3D kinematic surveys of brown dwarfs have largely focused on near-solar-metallicity, local thin disk populations (I. N. Reid et al. 2002; M. R. Zapatero Osorio et al. 2007; C. H. Blake et al. 2010; A. J. Burgasser et al. 2015b; C.-C. Hsu et al. 2021b, 2024a). The core limitation has been the need for high-resolution spectroscopy to measure radial velocities (RVs), restricting samples to relatively bright and nearby brown dwarfs (e.g., J or K $\lesssim$ 14.5–15.5 mag for Keck/Near-Infrared Spectrograph (NIRSPEC); C.-C. Hsu et al. 2021b). Nevertheless, these studies have provided important insights into the star formation and dynamical evolution of Galactic brown dwarfs. As late-M and L dwarfs are a mixture of low-mass stars and brown dwarfs, while late-L and T dwarfs are all brown dwarfs, their population velocity dispersions (see R. Wielen 1977; M. Aumer & J. J. Binney 2009) provide a clue to their ages and the Galactic star formation history at the very-low-mass end. One key finding was the early indication of a surprisingly old population of local L dwarfs, inconsistent with population simulations (C. H. Blake et al. 2010; A. J. Burgasser et al. 2015b). A more complete kinematic study of late-M, L, and T dwarfs within 20 pc by C.-C. Hsu et al. (2021b) resolved this discrepancy as being due to the contamination of unusually blue L dwarfs, an older and slightly metal-poor contaminant population (J. K. Faherty et al. 2009; A. J. Burgasser et al. 2015b). That study also revealed the first kinematic evidence of the stellar/substellar boundary around spectral type L4–L6, consistent with evolutionary models (I. Baraffe et al. 2003) and dynamical mass measurements (T. J. Dupuy & M. C. Liu 2017).[20] Population simulations applied to these kinematic data also indicate a low-mass star formation history consistent with exponential decline instead of a uniform star formation rate (see also, e.g., A. C. Day-Jones et al. 2013).

While the local sample includes members of older, more dispersed populations from the Milky Way's thick disk and halo, they are present at low relative numbers (12% and 0.5%; M. Jurić et al. 2008). Metal-poor L subdwarfs at the stellar/substellar boundary were identified in early surveys (A. J. Burgasser et al. 2003; A. J. Burgasser 2004; T. Sivarani et al. 2009; Z. H. Zhang et al. 2017, 2018) and shown to possess kinematics consistent with thick disk and halo populations (M. C. Cushing et al. 2009; N. Lodieu et al. 2015). More recently, several surveys have uncovered significantly metal-poor T- and Y-type brown dwarfs in the local volume (Z. H. Zhang et al. 2019; A. C. Schneider et al. 2020; A. M. Meisner et al. 2020, 2021; J. D. Kirkpatrick et al. 2021b; A. C. Schneider et al. 2021; A. J. Burgasser et al. 2025a), substantially expanding individual T subdwarf discoveries (B. Burningham et al. 2010; D. J. Pinfield et al. 2012), whose intrinsically faint magnitudes have made it difficult to obtain accurate astrometric and RV measurements. In addition, deep surveys with the Hubble Space Telescope (R. E. Ryan et al. 2005, 2011; B. W. Holwerda et al. 2014; R. E. Ryan et al. 2017; C. Aganze et al. 2022a) and more recently JWST (M. Nonino et al. 2023; A. J. Burgasser et al. 2024; B. W. Holwerda et al. 2024; K. N. Hainline et al. 2024; A. Y. A. Chen et al. 2025; Z. Tu et al. 2025a; K. N. Hainline et al. 2026; D. H. Li et al. 2026; S. J. Morrissey et al. 2026) have begun to reach thick disk and halo brown dwarfs at kiloparsec distances. The spectral morphologies of these low-temperature, metal-poor brown dwarfs provide a new stringent test of our understanding of cool atmospheres, brown dwarf evolution, and low-mass star formation (A. M. Meisner et al. 2021; E. Alvarado et al. 2024; R. Gerasimov et al. 2024a; S. Mukherjee et al. 2024).

The nearest brown dwarfs, while containing few metal-poor populations, enable the detailed photometric and spectroscopic measurements needed for Galactic archeology studies. Many of these sources have been validated with multiepoch astrometry and proper motion surveys (e.g., F. Marocco et al. 2021; A. M. Meisner et al. 2023; A. C. Schneider et al. 2023; F. Marocco et al. 2024; S. Karpov et al. 2025; A. C. Schneider et al. 2025; W. Zhang et al. 2025; F. Marocco et al. 2026) yielding 5D kinematic information. The last piece of the kinematics puzzle is the RV. While the faint magnitudes of these sources may limit our ability to obtain high-resolution spectroscopy, their highly structured spectra shaped by molecular absorption features enable RV precisions sufficient for kinematic studies ($\sigma_{\rm RV} \sim$ few km s^{-1}) with lower-resolution spectrographs ($R \approx$ 3000–6000).

In this work, we present a brown dwarf RV survey based on observations of 23 L-, T-, and Y-type nearby brown dwarfs across a range of metallicities, obtained with the JWST NIRSpec (P. Jakobsen et al. 2022). Section 2 describes our sample construction and observations, including updated proper motions for two sources in our sample. Section 3 illustrates our forward-modeling method to measure robust RVs, validated through comparison to high-resolution spectroscopic measurements in the literature. Section 4 presents our kinematic analysis, including *UVW* space motions, Galactic orbits, and population membership. We evaluate orbital energy and angular momentum to validate population assignments, as well as identify members of discrete Galactic substructures. Notable individual objects are discussed in Section 5. We summarize our findings in Section 6.

2. Sample and Observations

Our sample (Table 1) is drawn from nearby low-mass stars and brown dwarfs with L-, T-, and Y-type classifications observed with NIRSpec using its G395H high-resolution grating. We include both benchmark brown dwarf companions

[20] See the discussions in their Section 6.3 of C.-C. Hsu et al. (2021b) about the early determination of the stellar/substellar boundary at 2075 K, corresponding to L1–L2 by S. B. Dieterich et al. (2014).

Table 1
JWST NIRSpec/G359H Brown Dwarf Kinematics Sample

Name	Full Name	SpT	Cat.[a]	R.A. (deg)	Decl. (deg)	Parallax (mas)	μ_α (mas yr^{-1})	μ_δ (mas yr^{-1})	References
J0414−5854	CWISEP J041451.75−585454.0	esdT6	sd	63.716	−58.915	15 ± 4	212 ± 11	708 ± 12	(3), (17), (9)
J0415−0935	2MASSI J0415195−093506	T8	d	63.842	−9.583	175 ± 2	2214 ± 1	536 ± 1	(2), (6)
J0448−1935	WISE J044853.28−193548.6	sdT5	sd	72.224	−19.595	58 ± 3	901.1 ± 0.9	761.1 ± 0.9	(20), (12)
J0532+8246	2MASS J05325346+8246465	esdL8	sd	83.303	82.771	40.7 ± 0.5	2038.8 ± 0.6	−1663.0 ± 0.5	(3), (7)
J0645−6646	2MASS J06453153−6646120	d/sdT0	d/sd	101.371	−66.764	54 ± 3	−885 ± 2	1312 ± 2	(3), (12)
HIP 38939 B	2MASS J07580132−2538587	d/sdT4.5	d/sd	119.507	−25.651	54.16 ± 0.02	362.41 ± 0.01	−245.79 ± 0.02	(3), (7)
J0836−1859	WISE J083641.10−185947.0	d/sdT8	d/sd	129.171	−18.997	44 ± 2	−52.5 ± 0.8	−153.0 ± 0.8	(20), (12)
J1316+0755	ULAS J131610.28+075553.0	sdT6.5	sd	199.042	7.931	17 ± 3	−1026 ± 10	107 ± 10	(3), (5), (9)
J1416+1348 B	ULAS J141623.94+134836.3	sdT7	d/sd	214.1	13.81	107.7 ± 0.2	86.7 ± 0.3	128.0 ± 0.2	(3), (7)
J1416+1348 A	2MASS J14162408+1348263	d/sdL7	d/sd	214.101	13.808	107.7 ± 0.2	86.7 ± 0.3	128.0 ± 0.2	(4), (7)
HD 126053 B	ULAS J142320.79+011638.2	sdT7.5	sd	215.837	1.276	57.27 ± 0.04	223.53 ± 0.05	−478.28 ± 0.03	(3), (7)
HIP 70849 B	2MASS J14284235−4628393	T4.5	d	217.176	−46.478	41.46 ± 0.02	−44.05 ± 0.02	−201.58 ± 0.02	(13), (7)
GJ 576 B	ULAS J150457.65+053800.8	d/sdT5.5	d/sd	226.239	5.632	52.5 ± 0.02	−607.63 ± 0.02	−506.51 ± 0.02	(3), (7)
Gl 584 C	Gl 584 C	L8	d	230.845	30.248	56 ± 0.8	116.8 ± 0.4	−171.4 ± 0.5	(10), (18)
J1541−2250	WISE J154151.65−225024.9	Y1	d	235.464	−22.841	167 ± 2	−902.8 ± 0.9	−91.4 ± 0.9	(11), (12)
J1553+6933	WISE J155349.98+693355.2	sdT4	sd	238.459	69.565	26 ± 3	−1527 ± 12	1258 ± 13	(3), (16), (21)
J1626+3925	2MASS J16262034+3925190	usdL4	sd	246.576	39.423	32.3 ± 0.2	−1374.8 ± 0.2	237.4 ± 0.2	(19), (7)
J1810−1010	CWISEP J181006.00−101001.1	esdT3	sd	272.526	−10.167	112 ± 8	−1027 ± 4	−246 ± 4	(3), (14), (22)
J1828+2650	WISE J182831.08+265037.7	Y0	d	277.13	26.844	100 ± 2	1016.5 ± 0.8	169.3 ± 0.8	(11), (8)
Wolf 1130 C	Wolf 1130 C	sdT8	sd	301.335	54.409	60.3 ± 0.03	−1159.52 ± 0.04	−904.01 ± 0.03	(3), (7)
J2030+0749	2MASS J20304235+0749358	T1.5	d	307.68	7.826	102.8 ± 0.8	664.0 ± 0.9	−111.7 ± 0.9	(1), (7)
HN Peg B	HN Peg B	T2.5	d	326.12	14.768	55.15 ± 0.03	231.11 ± 0.03	−113.2 ± 0.03	(15), (7)
				Additional Literature: Metal-poor Brown Dwarf					
J1534−1043	WISEA J153429.75−104303.3	esdY	sd	233.622	−10.722	61 ± 5	−1253 ± 9	−2377 ± 7	(23), (24)

Notes.
[a] We organize our sample into three categories: benchmark solar-metallicity brown dwarfs (d), metal-poor brown dwarfs (sd), and mild subdwarfs (d/sd).

References—(1) W. M. J. Best et al. (2013); (2) A. J. Burgasser et al. (2002); (3) A. J. Burgasser et al. (2025a); (3) A. J. Burgasser et al. (2025a); (3) A. J. Burgasser et al. (2025a); (4) B. Burningham et al. (2010); (5) B. Burningham et al. (2014); (6) T. J. Dupuy & M. C. Liu (2012); (7) Gaia Collaboration et al. (2023); (8) C.-C. Hsu et al. (2021b); (9) This work; (10) J. D. Kirkpatrick et al. (2000); (11) J. D. Kirkpatrick et al. (2011); (12) J. D. Kirkpatrick et al. (2021a); (13) N. Lodieu et al. (2014); (14) N. Lodieu et al. (2022); (15) K. L. Luhman et al. (2007); (16) A. M. Meisner et al. (2020); (17) A. C. Schneider et al. (2020); (18) F. van Leeuwen (2007); (19) Z. H. Zhang et al. (2013); (20) Z. H. Zhang et al. (2019); (21) J.-Y. Zhang et al. (2025); (22) J.-Y. Zhang et al. (2025); (23) J. D. Kirkpatrick et al. (2021b); (24) J. K. Faherty et al. (2025).

with solar or near-solar metallicities and unassociated metal-poor brown dwarfs (subdwarfs "sd" and extreme subdwarfs "esd") in the field. The majority of the targets are drawn from JWST General Observer (GO) program GO-4668 (PI: Burgasser); we also include the T8 dwarf 2MASSI J0415195-093506 (J0415−0935; A. J. Burgasser et al. 2002; S. Alejandro Merchan et al. 2025) and the Y1 dwarf WISE J154151.65-225024.9 (J1541−2250; M. C. Cushing et al. 2011; J. D. Kirkpatrick et al. 2011) observed in GO-2124 (PI: Faherty), and the Y0 dwarf WISE J182831.08+265037.7 (J1828+2650; M. C. Cushing et al. 2011; J. D. Kirkpatrick et al. 2011; B. W. P. Lew et al. 2024) observed in program GO-1189 (PI: Roellig).

JWST/NIRSpec observations are summarized in Table 2. All sources were observed using NIRSpec's G395H grating and F290LP filter, providing moderate-resolution spectra ($\lambda/\Delta\lambda \approx 3{,}000$) over 2.9–5.1 μm. For program GO-4668, data were obtained using the S200A1 plus S200A2 slit combination, which covers the 3.7–3.8 μm gap between NIRSpec's two detectors. Data for programs GO-1189 and GO-2124 were obtained using only the S200A1 slit. We refer interested readers to B. W. P. Lew et al. (2024), J. K. Faherty et al. (2025), S. Alejandro Merchan et al. (2025), and A. J. Burgasser et al. (2025b) for full descriptions of the observations. All data were reduced using the JWST science calibration pipeline (versions 1.14.0, 1.15.1, 1.16.1, 1.17.1, 1.20.2) (H. Bushouse et al. 2026) and downloaded from the Mikulski Archive for Space Telescopes (MAST) Portal.[21] The signal-to-noise ratio (SNR) per pixel in the spectral band of interest (4.4–5.0 μm; see Section 3.1) ranges from 19 to 123, with a median of 56. It is noted that the reduced JWST NIRSpec G395H spectra are already corrected for barycentric (up to $\pm$30 km s^{-1}) and spacecraft velocities (up to $\pm$1 km s^{-1}), with the corrections stored as the "VELOSYS" keyword in the reduced FITS files for book-keeping purposes (priv. comm. Cheryl Pavlovsky).

For completeness, we also analyzed the kinematics for the metal-poor Y dwarf WISEA J153429.75−104303.3 (J1534−1043; aka "The Accident"; J. D. Kirkpatrick et al. 2021b) using the literature astrometry and RV measurements from J. K. Faherty et al. (2025).[22] Our findings of J1534−1043 are fully consistent with the halo kinematics indicated in J. K. Faherty et al. (2025), not associated with known dwarf galaxy merger remnants or streams.

2.1. New Proper Motion Measurements

For the majority of our sample, we used the highest precision measurements from the literature for parallax and proper motions (Table 1). For two sources, WISE J0414−5854 and ULAS J1316+0755, we report new and improved proper motion measurements based on combined astrometry from multiple surveys.

We then conducted a linear fit to all epochs to derive the proper motions, following the method described in A. C. Schneider et al. (2023, 2026). For J0414−5854, we combined seven z-band and y-band detections from NOIRLab Source Catalog (NSC) DR2 (D. L. Nidever et al. 2021), three J-band detections from VISTA Hemisphere Survey (VHS; R. G. McMahon et al. 2013), and 32 W1- and W2-band detections from Wide-field Infrared Survey Explorer (WISE)/unTimely (A. M. Meisner et al. 2023), spanning a total of 10.5 yr. Linear fits to the astrometry yield proper motions of $\mu_\alpha = 212 \pm 11$ mas yr^{-1} and $\mu_\delta = 708 \pm 12$ mas yr^{-1}, compared to $\mu_\alpha = 223 \pm 26$ mas yr^{-1} and $\mu_\delta = 672 \pm 24$ mas yr^{-1} reported in F. Marocco et al. (2021). For J1316+0755, early WISE/unTimely detections are blended with a background source, so we used only epochs after 2014 (13 detections). We combined this with eight UKIRT Infrared Deep Sky Survey (UKIDSS) Y- and J-band detections (A. Lawrence et al. 2007), spanning a total of 14 yr from 2006 (VHS) to 2020 (WISE). These data yield $\mu_\alpha = -1026 \pm 10$ mas yr^{-1} and $\mu_\delta = 107 \pm 10$ mas yr^{-1}, compared to $\mu_\alpha = -1012 \pm 15$ mas yr^{-1} and $\mu_\delta = 103 \pm 14$ mas yr^{-1} in B. Burningham et al. (2014). Our new proper motion measurements are fully consistent with literature values and show 1.4 to 2.4 times improvements in precision. We note that the quality of these imaging data was not sufficient to provide solid constraints on the trigonometric parallaxes of these two sources.

3. RV Measurements

3.1. Forward-modeling Method

The NIRSpec G395H data allow us to derive the full 6D phase space coordinates of our sources by providing the necessary RV. We deployed a forward-modeling approach based on the established method of modeling the highly structured CO first overtone (2−0) rotational-vibrational band at ∼2.3 μm in late-M, L, and T dwarf near-infrared spectra (e.g., C. H. Blake et al. 2007, 2010; A. J. Burgasser et al. 2015a, 2016; C.-C. Hsu et al. 2021b, 2023). Fortunately, NIRSpec G395H spectra encompass the similarly structured CO fundamental band from 4.4 to 5.0 μm (Figure 1). Our analysis is based on the method and the `SMART` code described in C.-C. Hsu et al. (2021b, 2023), excluding fitting to telluric absorption. Briefly, we used the Sonora Elf-Owl atmosphere models (S. Mukherjee et al. 2024) ($\lambda/\Delta\lambda \sim 60{,}000$), allowing for linear interpolation over effective temperature ($T_{\rm eff}$), surface gravity ($\log g$), metallicity ([M/H]), C/O ratio, and vertical eddy diffusion coefficient (κ_{zz}). The baseline model is modified by applying an RV shift and rotational broadening, the latter using the fast implementation kernel described in A. Carvalho & C. M. Johns-Krull (2023). The model is then convolved with a Gaussian instrumental line-spread function using the `PyAstronomy` "instrBroadGaussFast" function (S. Czesla et al. 2019), and resampled onto the wavelength grid of the data in the 4.4–5.0 μm band while preserving the total flux (using the `SMART` "integralResample" function). Additionally, we include an overall flux scale factor ($\sigma_{\rm flux}$) for the model, and a noise jitter term ($\sigma_{\rm noise}$) as a fraction of the observed flux added to the data error in quadrature. Model and observed spectra are compared using a chi-square statistic, with a second-order polynomial continuum correction applied to minimize this statistic. We used the Markov Chain Monte Carlo (MCMC) sampler `emcee` (D. Foreman-Mackey et al. 2013) to explore the parameter space and obtain best-fit values and uncertainties for the parameters and priors listed in Table 3. For this analysis, we deployed 100 MCMC walkers and 2000 total steps per walker, with the first 1000 steps discarded as burn-in.

[21] https://mast.stsci.edu/

[22] The spectra of J1534−1043 show SiH_4 absorption in the 4.4–4.8 μm (J. K. Faherty et al. 2025), so the Sonora Elf-Owl models used in this work are unable to provide a good fit to J1534−1043.

Table 2
NIRSpec Observations

Name	Desination (J2000)	W1 (mag)	W2 (mag)	GO ID	ID ID	Date of Obs. (UT)	Slit[a]	Exposure (s)	Reduction Version	SNR[b]
J0414−5854	J041451.80−585452.4	16.76 ± 0.03	15.36 ± 0.03	4668	72	2025-01-14	S200A1+S200A2	1538	1.16.1	48
J0415−0935	J041522.17−093457.1	15.15 ± 0.03	12.3 ± 0.01	2124	59	2022-10-16	S200A1	154	1.14.0	35
J0448−1935	J044853.70−193543.6	16.3 ± 0.03	14.23 ± 0.02	4668	103	2024-08-30	S200A1+S200A2	879	1.15.1	57
J0532+8246	J053312.61+824617.2	13.85 ± 0.01	13.27 ± 0.01	4668	19	2024-09-23	S200A1+S200A2	659	1.15.1	79
J0645−6646	J064529.10−664550.7	13.74 ± 0.02	13.3 ± 0.02	4668	10	2024-08-25	S200A1+S200A2	659	1.14.0	73
HIP 38939 B	J075801.75−253903.1	15.77 ± 0.04	13.86 ± 0.02	4668	101	2024-11-24	S200A1+S200A2	659	1.15.1	54
J0836−1859	J083641.13−185947.7	17.63 ± 0.09	15.13 ± 0.03	4668	106	2024-11-24	S200A1+S200A2	1319	1.15.1	19
J1316+0755	J131610.03+075551.5	16.54 ± 0.04	15.95 ± 0.06	4668	109	2025-02-19	S200A1+S200A2	1758	1.16.1	39
J1416+1348 B	J141623.96+134837.3	16.05 ± 0.03	12.83 ± 0.01	4668	43	2025-02-28	S200A1+S200A2	440	1.16.1	57
J1416+1348 A	J141624.16+134828.1	11.35 ± 0.02	11.02 ± 0.01	4668	6	2025-02-26	S200A1+S200A2	176	1.16.1	93
HD 126053 B	J142320.90+011635.3	17.9 ± 0.1	14.78 ± 0.02	4668	112	2025-02-28	S200A1+S200A2	1099	1.17.1	48
HIP 70849 B	J142842.28−462842.5	15.17 ± 0.02	13.84 ± 0.02	4668	85	2025-02-28	S200A1+S200A2	659	1.16.1	47
GJ 576 B	J150457.32+053756.8	16.21 ± 0.03	14.31 ± 0.02	4668	40	2025-02-28	S200A1+S200A2	879	1.16.1	53
Gl 584 C	J152322.78+301453.4	13.5 ± 0.01	13.02 ± 0.01	4668	80	2025-02-27	S200A1+S200A2	440	1.16.1	60
J1541−2250	J154151.41−225026.1	17.6 ± 0.2	14.22 ± 0.03	2124	5	2023-03-05	S200A1	673	1.14.0	34
J1553+6933	J155350.23+693355.7	17.07 ± 0.03	15.62 ± 0.03	4668	32	2024-11-21	S200A1+S200A2	1319	1.20.2	35
J1626+3925	J162618.23+392523.4	13.496 ± 0.009	13.165 ± 0.008	4668	26	2024-08-19	S200A1+S200A2	440	1.14.0	65
J1810−1010	J181006.12−101001.5	13.65 ± 0.02	12.483 ± 0.009	4668	35	2024-08-19	S200A1+S200A2	659	1.14.0	123
J1828+2650	J182831.08+265037.7	18.8 ± 0.2	14.39 ± 0.02	1189	11	2022-07-28	S200A1	2276	1.14.0	97
Wolf 1130 C	J200520.38+542433.9	17.16 ± 0.04	15.14 ± 0.02	4668	52	2024-08-30	S200A1+S200A2	1099	1.15.1	57
J2030+0749	J203043.10+074933.9	13.02 ± 0.02	12.2 ± 0.02	4668	29	2025-05-01	S200A1+S200A2	440	1.17.1	93
HN Peg B	J214428.75+144606.4	13.2 ± 0.03	12.6 ± 0.02	4668	83	2024-10-16	S200A1+S200A2	440	1.15.1	44

Notes.
[a] All data are observed using the G395H/F290LP grating/filter setting.
[b] The median SNR per pixel in the range 4.4–5.0 μm.

References—W1 and W2: J1810−1010: A. C. Schneider et al. (2020); Wolf 1130 C: J.-Y. Zhang et al. (2025); HN Peg B: AllWISE (R. M. Cutri et al. 2014); the rest of the sample: CatWISE (P. R. M. Eisenhardt et al. 2020) and CatWISE2020 (F. Marocco et al. 2021).

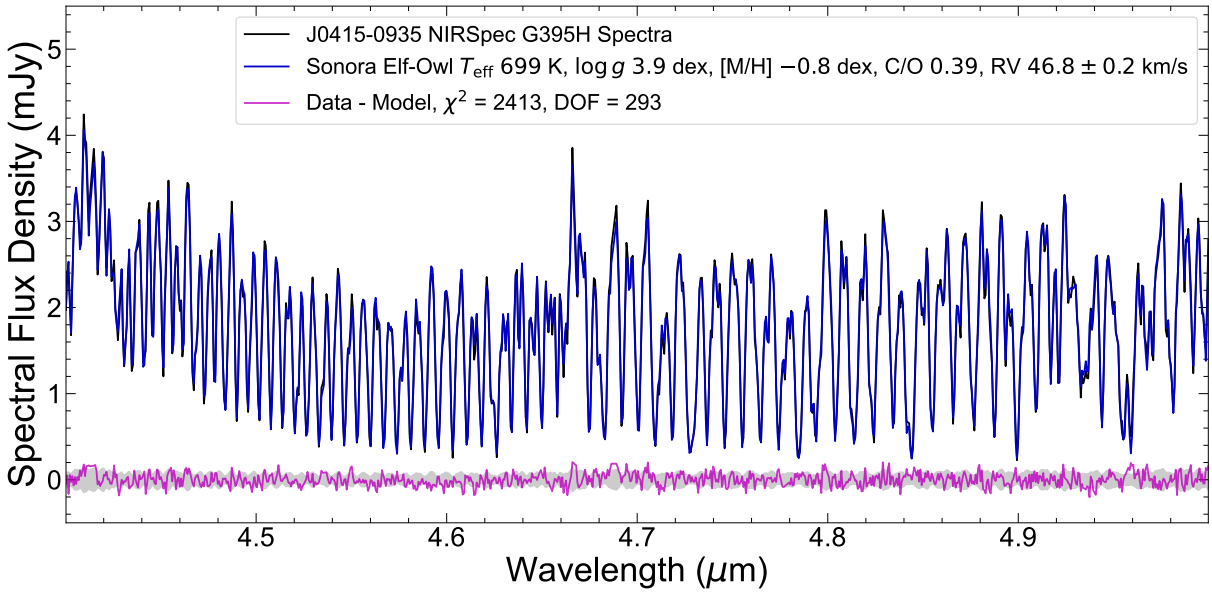


Figure 1. Example model fit to the JWST/NIRSpec G395H spectrum of the T8 dwarf J0415−0935, with relatively low SNR ∼35 compared to our full sample (Table 2). The observed spectrum is shown in black, with the corresponding ±1σ uncertainty indicated by the gray shaded region centered at zero. The best-fit Sonora Elf-Owl model (S. Mukherjee et al. 2024) is shown in blue, and the difference spectrum (data − model) is shown in magenta. The majority of structure observed in this region arises from the CO (1−0) fundamental band, which is used to anchor our RV measurements. Fits for each source in our full sample (22 objects) are provided as a figure set in the online journal.

(The complete figure set (22 images) is available in the online article.)

Table 3
Forward Modeling Parameters

Description	Symbol (unit)	Priors[a]	Bounds
Temperature	$T_{\rm eff}$ (K)	(300, 1400)	(300, 2400)
Surface gravity	log g (cm s^{-2})	(3.23, 5.5)	(3.23, 5.5)
Metallicity	[M/H] (dex)	(−1.0, +1.0)	(−1.0, +1.0)
C/O	C/O[b]	(0.229, 1.145)	(0.229, 1.145)
Vertical diffusion	κ_{zz} (cm^2 s^{-1})	(10^2, 10^8)	(10^2, 10^8)
Rotational velocity	$v \sin i$ (km s^{-1})	(0, 200)	(0, 200)
RV	RV (km s^{-1})	(−250, +250)	(−400, +400)
Resolution	R	(1500, 4000)	(1500, 4000)
Flux Scaling	$\sigma_{\rm flux}$	(0.0, 1.0)	(0.0, 1.0)
Noise Jitter	$\sigma_{\rm noise}$	(0.0, 0.5)	(0.0, 0.5)

Notes.
[a] All priors assume a uniform distribution over the range specified.
[b] The solar elemental abundance of C/O = 0.458, so our priors correspond to 0.5 to 2.5 × the solar C/O value (K. Lodders et al. 2009; S. Mukherjee et al. 2024).

Figure 1 illustrates an example fit for the T8 dwarf J0415−0935. The best-fit physical parameters are labeled in the legend, with sampling uncertainties without systematics across various models. Our $T_{\rm eff} = 699^{+2}_{-4}$ K is fully consistent with the $T_{\rm eff}$ = 677 ± 56 K from J. C. Filippazzo et al. (2015). However, our log g = 3.9 cgs dex differs significantly from the log g = 4.8 ± 0.5 cgs dex in J. C. Filippazzo et al. (2015), and metallicity [M/H] = −0.8 dex is unphysical given that J0415−0935 is a solar-metallicity T dwarf standard (A. J. Burgasser et al. 2006). Indeed, fitting the relatively narrow wavelength range generally exhibits systematic biases across several studies in the literature, especially high-resolution spectroscopic studies focused on optimizing the RV measurements (see C. Del Burgo et al. 2009; C.-C. Hsu et al. 2021b, 2024a, 2024b). However, the main goal of this study is to obtain a reliable and robust RV measurement, and the core of RV measurements is to obtain the best spectral template that matches the observed spectra. While there are slight mismatches at 4.40–4.42 μm and 4.66–4.70 μm, our best-fit model shows a reasonable fit to the observed spectra, with a reduced $\chi^2 \sim$ 8.07 (without the error jitter term). From this analysis, we obtained a best-fit RV = 46.8 ± 0.2 km s^{-1}, where the uncertainty reflects the statistical distribution from our Bayesian posterior. To explore whether different $T_{\rm eff}$, log g, and metallicity would bias our resulting RV, we conducted a restricted MCMC forward-modeling routine for J0415−0935, under the same method but fixing $T_{\rm eff}$ = 677 K, log g = 4.83 cgs dex, and solar metallicity from J. C. Filippazzo et al. (2015). This experiment measured an RV = $46.8^{+0.4}_{-0.3}$ km s^{-1}, fully consistent with our reported best-fit RV (46.8 ± 0.2 km s^{-1}), though with ∼1.5× larger uncertainty and a significantly poorer fit ($\chi^2 \approx$ 6335). This demonstrates that the CO and H_2O lines provide a robust RV anchor even if their atmospheric parameters might not be fully accurate.

For most of our sample, statistical errors are below 0.5 km s^{-1}; the two exceptions are the extremely metal-poor subdwarfs usdL4 J1626+3925 and esdT3 J1810−1010, which have weak molecular absorption features and higher statistical errors of 1 km s^{-1}. As discussed below, we include an additional 5 km s^{-1} systematic uncertainty to the measurement to account for calibration effects, which is 20 times smaller than the native resolution of the spectrum (or 1/10$^{\rm th}$ of the pixel). The combined value, 47 ± 5 km s^{-1}, is fully consistent with the best ground-based measurement of RV = 51.9 ± 1.1 km s^{-1} reported by C.-C. Hsu et al. (2021b) based on high-resolution ($\lambda/\Delta\lambda \approx$ 25,000) Keck/NIRSPEC observations; and with the RV = 47.1 ± 1.8 km s^{-1} reported by S. Alejandro Merchan et al. (2025) using the same JWST NIRSpec G395H spectra (which they used different wavelength segments and three substellar atmosphere models).

3.2. New High-resolution Spectroscopic RV Measurements

We also present new RV measurements for J1416+1348 A using Keck/NIRSPEC high-resolution spectra (I. S. McLean et al. 1998, 2000). Our NIRSPEC data for J1416+1348 A were observed on 2015 December 29 (UT) (PI: Burgasser) under excellent conditions, with clear sky and excellent seeing of 0.″44. The N7 filter (corresponding to the K band) and the $0.''432 \times 12$ slit were selected. The spectra were taken under two 500-s exposures in an AB nodding pair. We also observed the A0V star HD 35505 to serve as our wavelength calibrator. The data were reduced using the modified `NSDRP` code (H. D. Tran et al. 2016) detailed in C.-C. Hsu et al. (2021b) and C. A. Theissen et al. (2022).

The reduced spectra were then forward-modeled following the prescription of C.-C. Hsu et al. (2021b, 2023) using `SMART` (C.-C. Hsu et al. 2021a) and the MCMC `emcee` sampler (D. Foreman-Mackey et al. 2013). We chose the BT-Settl atmosphere models (F. Allard et al. 2012) and ESO Earth atmosphere models (S. Moehler et al. 2014). Our best-fit parameters for J1416+1348 A are RV $= -42.3 \pm 0.4$ km s^{-1}, $T_{\rm eff} = 1731^{+21}_{-20}$ K, $\log g = 5.50^{+0.02}_{-0.04}$ cgs dex, and $v \sin i = 40.2 \pm 0.6$ km s^{-1}.

3.3. Validation of RV Measurements

Our RV measurements range from -260 km s^{-1} to $+130$ km s^{-1}, larger than the typical range ($|\mathrm{RV}| \leqslant 80$ km s^{-1}) for nearby thin disk low-mass stars and brown dwarfs (C. H. Blake et al. 2010; C.-C. Hsu et al. 2021b, 2024a). To validate these RVs, we compared them to available literature measurements summarized in Table 4. In general, high-resolution ($\lambda/\Delta\lambda > 20{,}000$) spectroscopic RVs are the most reliable measurements, as the molecular lines are well-resolved and calibration is typically reliable to 0.1–0.5 km s^{-1} (C.-C. Hsu et al. 2021b, 2024a). However, given the faintness of our sources, we also included medium-resolution ($3000 \lesssim \lambda/\Delta\lambda \lesssim 6000$) measurements where available.

Figure 2 illustrates this comparison. We find overall agreement between our NIRSpec RVs and high-resolution RVs from the literature, with a median difference (literature RV−NIRSpec RV) of $+5.1 \pm 2.1$ km s^{-1}. The source with the largest RV disagreement, the sdT4 J1553+6933, has a very-low-precision measurement (-110 ± 90 km s^{-1}) based on moderate-resolution spectra (A. J. Burgasser et al. 2025a), and we discount that measurement from our analysis.[23] In particular, the medium-resolution $R \sim 2700$ Keck/NIRES spectra of J1553+6933 from (A. J. Burgasser et al. 2025a) have lower SNRs and telluric absorption from the ground, and the Keck/NIRES wavelength calibration is less reliable than the JWST NIRSpec G395H wavelength used in this study. The marginal systematic offset, with individual values ranging between $+0.3$ km s^{-1} and $+7.1$ km s^{-1} (i.e., our JWST NIRSpec RVs are systematically more negative compared to the literature high-resolution RVs), may be due to the pipeline wavelength calibration of NIRSpec data. Our finding here is consistent with the JWST validation report on individual emission lines from unresolved, high-velocity planetary nebulae, and indicates an uncertainty of $\sim$6 km s^{-1} for G395H spectroscopy (K. Glidic et al. 2025). Indeed, subpixel centering offsets of sources with the NIRSpec slit can result in velocity shifts of the same scale; a 0.1 pixel offset corresponds to a shift of approximately 5 km s^{-1}. Thus, we adopt a systematic RV uncertainty of 5 km s^{-1} to our measurements for the remainder of the analysis.

We also explored systematic errors driven by the choice of wavelength region used to measure our RVs. For every spectrum, we computed RVs using our forward-modeling method with bins of 0.6 μm in steps of 0.1 μm, similar to the wavelength bin size used in our fitting routine, across the full 2.9–5.7 μm range of the G395H data. Results of this analysis are shown in Figure 3. There is a consistent offset and larger uncertainties for RVs derived at bluer wavelengths ($\lambda < 3.8$ μm), but in the region of the CO band these differences level off at zero. The larger uncertainties at wavelengths outside the CO band can be attributed to the absence of strong, dense, and well-structured molecular opacity features, particularly near the 4 μm flux peak, whereas errors and offsets at shorter wavelengths may arise from saturated CH_4 absorption centered at 3.3 μm (which generally show lower SNR than CO band at 4.5 μm) for the T and Y dwarfs in the sample (see J. K. Faherty et al. 2024; B. W. P. Lew et al. 2024), and/or wavelength-dependent systematics from the JWST wavelength calibration model.

While RV measurements of young cool stars are impacted by stellar activity ($\sim$1–2 km s^{-1}; e.g., M. A. Gully-Santiago et al. 2017; S.-Y. Tang et al. 2024), our sample is largely T and Y dwarfs at field ages and much cooler temperatures ($\lesssim$1200 K). Although brown dwarf variability is commonly found in young L-type brown dwarfs (J. M. Vos et al. 2022), older and cool T/Y dwarfs show much less RV variability from high-resolution spectra (C.-C. Hsu et al. 2021b). A well-known young early T dwarf, J0136+0933 RV variations are $\lesssim$2 km s^{-1} (C.-C. Hsu et al. 2021b), so our old brown dwarfs are expected to have RV variations less than this level (unless they are in a close binary; C.-C. Hsu et al. 2023; J. W. Xuan et al. 2024; S. Whitebook et al. 2026), and our systematic RV uncertainty of 5 km s^{-1} is larger than these RV variations.

In summary, we find good agreement between RVs measured for L, T, and Y dwarfs between JWST/NIRSpec G395H observations and high-resolution spectroscopic observations to within a 5 km s^{-1} systematic uncertainty, corresponding to 1/20th of the resolution of the data.

4. Ancient Brown Dwarf Kinematics

4.1. UVW Velocities

Combining astrometry with our measured RVs, we computed the Galactic *UVW* space motions of the sources in our sample following the prescription described in C.-C. Hsu et al. (2021b). We used the D. R. H. Johnson & D. R. Soderblom (1987) formulation to derive *UVW* space motions, as implemented in the `SMART` function `compute_uvw_velocity` (C.-C. Hsu et al. 2021a). The D. R. H. Johnson & D. R. Soderblom (1987) formulation is a right-handed spherical coordinate system, where U is the velocity toward the Galactic center, V is the velocity along the Galactic rotation, and W is the velocity toward the Galactic north pole. We applied a heliocentric correction to place our *UVW* space motions at the local standard of rest (LSR) using the solar LSR

[23] The currently known (noncontacting) shortest orbital period ultracool dwarf binary LP 413-53 has a maximum RV difference of $\sim$52 km s^{-1}, with a period of 17 hr and separation $a < 20$ stellar radii (C.-C. Hsu et al. 2023).

Table 4
Measured RVs and Derived UVW Velocities

Name	RV[a] (km s^{-1})	RV_{lit} (km s^{-1})	RV_{lit} Reference	U (km s^{-1})	V (km s^{-1})	W (km s^{-1})	Pop.[c]
J0414−5854	$130.3^{+0.4}_{-0.5} \pm 5$	⋯	⋯	-224 ± 68	-76 ± 5	-89 ± 5	TD/Halo
J0415−0935	$46.8 \pm 0.2 \pm 5$	52 ± 1	(4)	-51 ± 4	-30 ± 2	24 ± 3	D
J0448−1935	$92.0 \pm 0.3 \pm 5$	⋯	⋯	-109 ± 5	-41 ± 3	28 ± 5	D/TD
J0532+8246	$-173.4 \pm 0.2 \pm 5$	-172 ± 1	(8)	-61 ± 4	-329 ± 4	57 ± 3	Halo
J0645−6646	$-25.4 \pm 0.3 \pm 5$	-33 ± 10[b]	(10)	-122 ± 7	43 ± 5	-32 ± 3	TD
HIP 38939 B	$-14.0 \pm 0.2 \pm 5$	-8.2 ± 0.1	(2)	49 ± 2	9 ± 5	22.5 ± 0.2	D
J0836−1859	$21.6^{+0.5}_{-0.6} \pm 5$	⋯	⋯	9 ± 2	-14 ± 4	-2 ± 1	D
J1316+0755	$24.8 \pm 0.4 \pm 5$	⋯	⋯	-229 ± 44	-137 ± 25	68 ± 8	TD/Halo
J1416+1348 B	$-51.5 \pm 0.2 \pm 5$	⋯	⋯	-10 ± 2	17.8 ± 0.1	-40 ± 5	D
J1416+1348 A	$-48.2 \pm 0.2 \pm 5$	-42.3 ± 0.4	(5)	-9 ± 2	17.9 ± 0.1	-37 ± 5	D
HD 126053 B	$-24.8 \pm 0.3 \pm 5$	-19.21 ± 0.03	(9)	30 ± 3	-2.3 ± 0.6	-37 ± 4	D
HIP 70849 B	$-4.9 \pm 0.2 \pm 5$	-0.13 ± 0.03	(9)	2 ± 4	2 ± 3	-13 ± 1	D
GJ 576 B	$-89.8 \pm 0.2 \pm 5$	-84.8 ± 0.1	(3)	-50 ± 3	-63.1 ± 0.3	-54 ± 4	TD
Gl 584 C	$-13.8 \pm 0.2 \pm 5$	-7.2 ± 0.2	(9)	22 ± 2	4 ± 2	-10 ± 4	D
J1541−2250	$-38.7 \pm 0.4 \pm 5$	⋯	⋯	-34 ± 4	2 ± 1	4 ± 2	D
J1553+6933	$-162.7 \pm 0.4 \pm 5$	110 ± 90[b]	(1)	-171 ± 43	-209 ± 21	-42 ± 12	Halo
J1626+3925	$-256.6^{+0.9}_{-1.0} \pm 5$	-239 ± 12[b]	(6)	-163 ± 2	-264 ± 3	-26 ± 4	Halo
J1810−1010	$-85.2^{+0.9}_{-1.1} \pm 5$	-85 ± 13[b]	(11)	-62 ± 5	-45 ± 3	34 ± 2	D/TD
J1828+2650	$-30.9 \pm 0.2 \pm 5$	⋯	⋯	-20 ± 3	12 ± 4	-41 ± 2	D
Wolf 1130 C	$-37.8 \pm 0.3 \pm 5$	-33 ± 1	(7)	117.6 ± 0.1	-36 ± 5	40 ± 1	TD
J2030+0749	$-28.3 \pm 0.1 \pm 5$	-21.2 ± 0.7	(4)	-20 ± 3	-9 ± 4	-11 ± 2	D
HN Peg B	$-19.8 \pm 0.2 \pm 5$	-20 ± 1	(4)	-4 ± 2	-11 ± 4	-2 ± 2	D
Additional Literature Metal-poor Brown Dwarf							
J1534−1043	⋯	-116 ± 5	(12)	-66 ± 4	-181 ± 17	-110 ± 5	Halo

Notes.
[a] The RV uncertainties are reported in the order of sampling uncertainty and the systematic uncertainty of 5 km s^{-1}.
[b] Measurements based on moderate-resolution data ($3000 \lesssim \lambda/\Delta\lambda \lesssim 6000$), which were ignored in our validation analysis.
[c] Galactic kinematic populations, including thin disk (D), thick disk (TD), and halo (H). See Section 4.1 for the full definition.
[d] While J1316+0755 shows halo kinematics using the T. Bensby et al. (2003) formulation, it is assigned as a transitional thick disk/halo member from our analysis of Galactic total energy and Galactic angular momentum (Section 4.3).
References—(1) A. J. Burgasser et al. (2025a); (2) Gaia Collaboration et al. (2023); (3) J.-L. Halbwachs et al. (2018); (4) C.-C. Hsu et al. (2021b); (5) This work; (6) N. Lodieu et al. (2015); (7) G. N. Mace et al. (2018); (8) A. Reiners & G. Basri (2006); (9) C. Soubiran et al. (2018); (10) Z. H. Zhang et al. (2018); (11) J.-Y. Zhang et al. (2025); (12) J. K. Faherty et al. (2025).

velocity (U, V, W) = (11.1, 12.24, 7.25) km s^{-1} from R. Schönrich et al. (2010).

From these velocities, we computed Galactic population probabilities using the velocity dispersions introduced in T. Bensby et al. (2003). Galactic population probabilities of the thick disk to thin disk probability ratio $P(\mathrm{TD})/P(\mathrm{D})$ and halo to thick disk probability $P(\mathrm{Halo})/P(\mathrm{TD})$ are computed using the `SMART` function "compute_galactic_pop_prob." Thin disk membership is assigned for $P(\mathrm{TD})/P(\mathrm{D}) < 0.1$; thick disk membership is assigned for $P(\mathrm{TD})/P(\mathrm{D}) > 10$; intermediate thin disk/thick disk membership is assigned for $0.1 < P(\mathrm{TD})/P(\mathrm{D}) < 10$. Halo membership is assigned for $P(\mathrm{Halo})/P(\mathrm{TD}) > 10$, and intermediate thick disk/halo membership is assigned for $0.1 < P(\mathrm{Halo})/P(\mathrm{TD}) < 10$. The derived velocities and kinematic population memberships for our sample are summarized in Table 4. We note that both J0414−5854 and J1316+0755 lack trigonometric parallaxes, so velocities and kinematic memberships are based on estimated distances from A. C. Schneider et al. (2020) and B. Burningham et al. (2014), respectively.

We further evaluated the *UVW* space motions of our sample by comparing them to previously identified stellar populations. In particular, we considered the Galactic thin disk stars curated from the Gaia Catalogue of Nearby Stars (GCNS) Gaia Collaboration et al. (2021), thick disk stars from L. Duong et al. (2018), halo stars from P. E. Nissen et al. (2024), Helmi stream members from H. H. Koppelman et al. (2019) and M. A. Limbach et al. (2021), Thamnos stream members from R. Xie et al. (2026), and members of the Gaia-Enceladus (GSE) dwarf galaxy merger from H. Ernandes et al. (2024). For GCNS, we restricted the GCNS sample to RV errors less than 0.5 km s^{-1} and RUWE < 1.3, and selected sources with thin disk membership based on their Galactic kinematic membership probability (see Section 4.1) using the same method as in T. Bensby et al. (2003). Where necessary, we updated the astrometry and RVs for these sources using data from Gaia DR3 (Gaia Collaboration et al. 2023), and computed LSR *UVW* velocities in the same manner as our brown dwarf sample.

Figure 4 illustrates the *UVW* space motions of our brown dwarfs and the literature samples. The majority of our sample (12 out of 23 sources) are aligned with the Galactic thin disk, in particular our solar-metallicity benchmark companion sources. Our transitional thin disk/thick disk sources (J0448−1935 and J1810−1010) and thick disk sources (J0645−6646, GJ 576 B, and Wolf 1130 C) clump near the thin disk

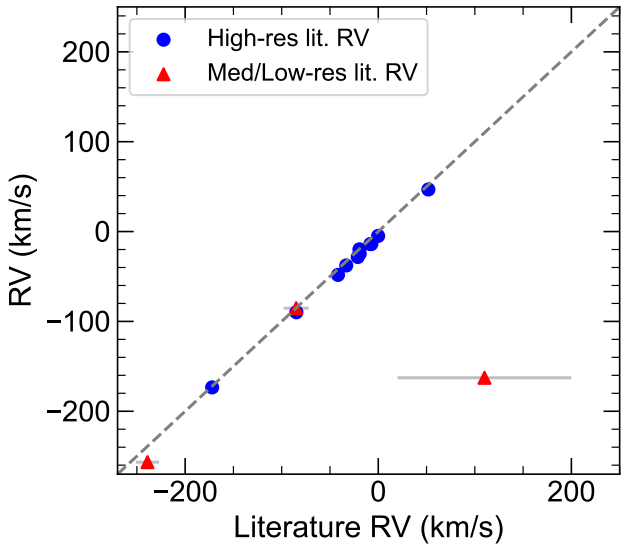


Figure 2. Comparison of our NIRSpec RV measurements with high-resolution ($\lambda/\Delta\lambda > 20{,}000$; blue circles) and moderate-resolution ($3000 < \lambda/\Delta\lambda < 10{,}000$; red triangles) spectroscopic measurements from the literature. The dashed line indicates perfect agreement. The source with the largest disagreement is J1553+6933, which has a very-low-precision measurement (-110 ± 90 km s^{-1}) based on moderate-resolution spectra (A. J. Burgasser et al. 2025a). Our RV measurements show excellent agreement with the literature high-resolution RVs (standard deviation of 2.3 km s^{-1} and median difference of -5.1 km s^{-1}, demonstrating that our method is robust using G395H at 4.4–5.0 μm at $R \sim 3000$ resolution.

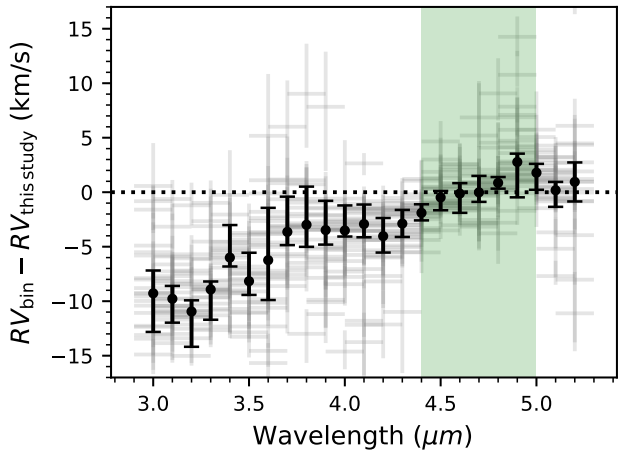


Figure 3. Difference between RVs measured at different wavelength bins (RV_{bin}; 0.6 μm bin size in steps of 0.1 μm) and the RV adopted in this study based on the CO band ($RV_{this\ study}$; green shaded region, 4.4–5.0 μm), across the entire NIRSpec G395H wavelength range. Gray points show individual RV measurements for each source in each 0.6 μm bin, whereas black points with error bars indicate the median and 25th to 75th percentiles for each bin across all sources. There is a clear shift toward more negative RVs at shorter wavelengths, but around the CO-band region used for our analysis, RV values are roughly constant with wavelength.

locus but extend outward toward higher velocities. Our transitional thick disk/halo sources (J0414−5854 and J1316+0755[24]) both appear to overlap with Helmi stream members in the Toomre diagram and marginally in the *U*–*V* plane. However, they are highly inconsistent with the Helmi stream in the *U*–*W* and *V*–*W* planes. Additionally, we note that both J0414−5854 and J1316+0755 lack trigonometric parallaxes, so more robust parallaxes could help anchor their true kinematic membership and origins. Our halo sources are widely scattered in each of the *UVW* planes, with J1553+6933 overlapping with Gaia-Enceladus members (see A. M. Meisner et al. 2026), J0532+8246 overlapping with Thamnos members (see A. J. Burgasser et al. 2025a), and J1626+3925 and J1534−1043 appearing to be general halo members. These potential memberships are evaluated further in Section 4.3.

4.2. Galactic Orbits

We assessed the Galactic orbits for our sample using `galpy` (J. Bovy 2015), following the approach described in C.-C. Hsu et al. (2021b, 2024a). We adopted the isocylindrical Galactic potential model of P. J. McMillan (2017)[25], assuming a solar azimuthal velocity of 233.1 km s^{-1}, a solar Galactic radius and vertical height ($R_\odot$, $Z_\odot$) = (8.21, 0.014) kpc (P. J. McMillan 2017), and the LSR solar motion from R. Schönrich et al. (2010) used to compute brown dwarf *UVW* velocities. Orbit integrations spanned −5 Gyr to +5 Gyr relative to the present with a time step of 2 Myr. We parameterized the resulting orbits through their minimum and maximum Galactic cylindrical radius (R_{max}, R_{min}), maximum absolute Galactic vertical height ($|Z|$), median orbit eccentricity ($e \equiv \langle R_{max} - R_{min}\rangle / \langle R_{max} + R_{min}\rangle$), and median absolute orbit inclination ($\tan i \equiv |Z/\sqrt{X^2 + Y^2}|$), where *XYZ* are Galactic Cartesian coordinates aligned with our *UVW* velocity components. Uncertainties in astrometry and RV measurements were propagated using 100 Monte Carlo realizations of the Galactic orbits for each source.

The inferred Galactic orbital parameters are summarized in Table 5. The majority of our thin disk sources have flat ($|Z| \lesssim 300$ pc, $i \lesssim 2°$), near-circular orbits ($R_{min} \approx R_\odot \gtrsim 7$ kpc, $R_{max} \approx R_\odot \lesssim 10$ kpc, $e \lesssim 0.15$), consistent with other local brown dwarfs (A. J. Burgasser et al. 2015b; C.-C. Hsu et al. 2021b, 2024a). The one exception is the HD 126053 subdwarf system, which has $|Z| = 670$ pc ($i = 4.°5$) despite having a low radial eccentricity. Compared to these sources, our thick disk and halo objects have progressively larger orbital eccentricities (median values: thin disk = 0.09, thick disk = 0.38, halo = 0.81) and inclinations (thin disk = 1.°9, thick disk = 6°, halo = 27°), consistent with scattering from or formation outside the thin disk. The radial motions of the thick disk and halo objects naturally divide into two categories: "inbound" ($R_{min} \lesssim 7$ kpc, $R_{max} \approx R_\odot \lesssim 10$ kpc) and "passing through" ($R_{min} \lesssim 7$ kpc, $R_{max} \gtrsim 10$ kpc). Notably, the three sources with retrograde orbits ($L_z < 0$, see below) are largely on inbound orbits, with J1553+6933 and J1626+3925 diving deeply into the bulge ($R < 1$ kpc) on near-radial trajectories ($e \approx 0.9$). In contrast, the thick disk dwarf and halo dwarf J0645−6646 and J1553+6933 have extreme outbound orbits extending to 15–20 kpc from the Galactic center (see M. C. Cushing et al. 2009).

4.3. Galactic E_{tot}–L_z Analysis

While *UVW* velocity components are convenient for assessing kinematic membership and tracing orbital motion,

[24] J1316+0755 shows halo kinematics from T. Bensby et al. (2003) metrics, but in Section 4.3 we show that it is most consistent with thick disk membership, so it is designated as thick disk/halo.

[25] The Miyamoto–Nagai potential was used in several brown dwarf kinematics studies (A. J. Burgasser et al. 2015b; C.-C. Hsu et al. 2021b, 2024a). To be fully consistent with our analysis in Section 4.3, we use the P. J. McMillan (2017) potential, which also includes a halo component.

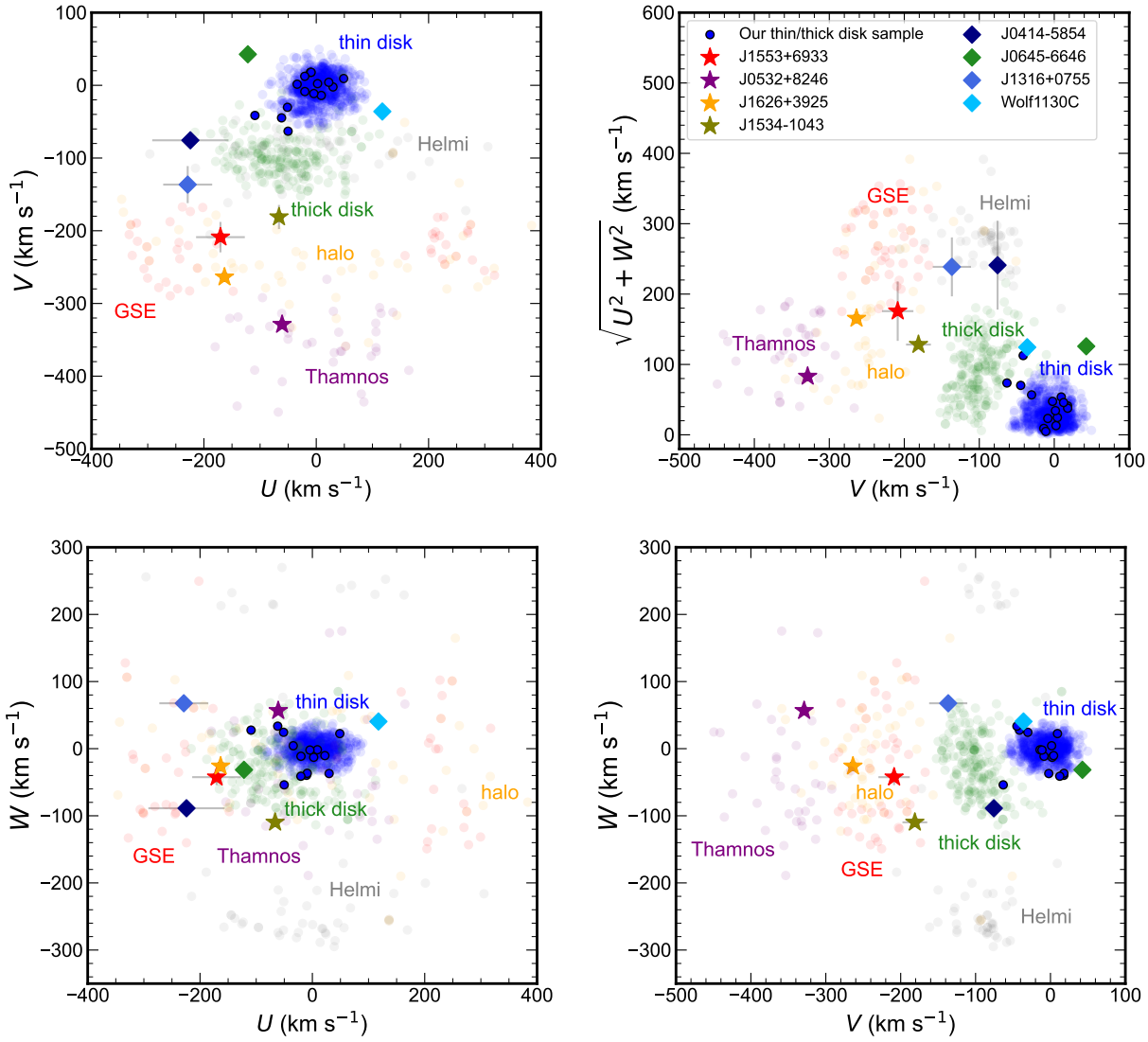


Figure 4. *UVW* space motions and Toomre diagram for our sample. Individual sources indicated in the legend are labeled as stars (halo members) or diamonds (thick disk/halo members), whereas the remaining sources in our sample are shown as large blue dots with black outlines. Uncertainties are plotted, but are generally smaller than the marker size. *UVW* velocities for stars in labeled Galactic populations and substructures are also shown, including thin disk stars from Gaia Collaboration et al. (2021, blue), thick disk stars from L. Duong et al. (2018, green), halo stars from (P. E. Nissen et al. 2024, orange), Helmi stream members from H. H. Koppelman et al. (2019) and M. A. Limbach et al. (2021, gray), Thamnos members from R. Xie et al. (2026, purple), and Gaia-Enceladus (GSE) members from H. Ernandes et al. (2024, red).

they are not conserved across the Galactic potential, making it difficult to compare stars in different regions across the Milky Way. For this reason, total orbital energy $E_{\rm tot}$ and vertical angular momentum L_z are better parameters for identifying and assessing membership in Galactic populations and substructures (A. Helmi 2020). We computed these quantities using `galpy`, assuming the P. J. McMillan (2017)[26] Galactic potential, propagating uncertainties using 100 Monte Carlo samples. In addition to our brown dwarfs, we also computed these quantities for the Galactic population samples described in Section 4.1. To ensure robust membership for these samples, we limited thin disk, thick disk, and halo populations to those that satisfy the T. Bensby et al. (2003) probability criteria (Section 4.1), and constrained the Gaia-Enceladus and Helmi samples to those sources with propagated uncertainties $\sigma(E_{\rm tot}) < 1000$ km^2 s^{-2} and $\sigma(L_z) < 100$ kpc km s^{-1}.

Figure 5 illustrates the $E_{\rm tot}$–L_z space for these sources. As expected, our solar or near-solar-metallicity brown dwarfs are fully consistent with the thin disk population from Gaia, while our two transitional thin/thick disk sources, J0448−1935 and J1810−1010, lie in an overlapping space between the thin disk and thick disk samples. Two of our thick disk sources, Wolf 1130 C and GJ 576 B, are in line with the bulk of the thick disk population, whereas J0645−6646 resides at the high-energy, high-angular-momentum tail of this distribution. Among the brown dwarfs exhibiting halo kinematics, J1553+6933 aligns well in $E_{\rm tot}$–L_z space with Gaia-Enceladus members, as also reported in A. M. Meisner et al. (2026); it can be firmly ruled out as a Helmi member as proposed by A. J. Burgasser et al. (2025a). We also confirm the L subdwarf J0532+8246 as a likely member of Thamnos based on these quantities proposed in A. J. Burgasser et al. (2025a). J1626+3925 and J1534

[26] The Galactic potential used to select the Galactic halo and substructures from R. P. Naidu et al. (2020) is P. J. McMillan (2017), and to compare their results with our sample, the same Galactic potential is necessary.

Table 5
Galactic Orbital Parameters

Name	Pop.[a]	$R_{\rm min}$ (kpc)	$R_{\rm max}$ (kpc)	$\lvert Z\rvert$ (kpc)	e	i (deg)	$E_{\rm tot}$ (km^2 s^{-2})	L_z (kpc km s^{-1})
J0414−5854	TD/Halo	$4.22^{+0.14}_{-0.08}$	$8.5^{+0.2}_{-0.1}$	$1.96^{+0.27}_{-0.09}$	$0.34^{+0.01}_{-0.02}$	$17.0^{+1.6}_{-0.5}$	-168456^{+568}_{-573}	1304 ± 27
J0415−0935	D	5.9 ± 0.1	$8.79^{+0.06}_{-0.05}$	$0.42^{+0.05}_{-0.07}$	0.19 ± 0.01	$3.1^{+0.4}_{-0.5}$	-162012^{+234}_{-214}	1724 ± 13
J0448−1935	D/TD	$4.9^{+0.1}_{-0.13}$	10.3 ± 0.1	0.6 ± 0.1	0.36 ± 0.01	$4.0^{+0.7}_{-0.9}$	-159465^{+427}_{-376}	1637^{+24}_{-20}
J0532+8246	Halo	2.2 ± 0.1	$8.48^{+0.05}_{-0.06}$	$1.57^{+0.07}_{-0.09}$	0.59 ± 0.02	19^{+1}_{-2}	-175975^{+434}_{-453}	-742^{+42}_{-27}
J0645−6646	TD	6.76 ± 0.09	$15.9^{+0.8}_{-0.6}$	0.9 ± 0.1	0.41 ± 0.02	$3.7^{+0.5}_{-0.4}$	-138271^{+1503}_{-1691}	2326^{+32}_{-39}
HIP 38939 B	D	$7.29^{+0.04}_{-0.07}$	$10.1^{+0.2}_{-0.3}$	$0.411^{+0.005}_{-0.006}$	$0.162^{+0.009}_{-0.013}$	$2.52^{+0.04}_{-0.02}$	-153201^{+1228}_{-1125}	2047^{+37}_{-35}
J0836−1859	D	$7.2^{+0.2}_{-0.3}$	$8.21^{+0.05}_{-0.04}$	$0.031^{+0.011}_{-0.005}$	$0.068^{+0.016}_{-0.008}$	$0.23^{+0.08}_{-0.03}$	-159968^{+898}_{-1107}	1860^{+32}_{-41}
J1316+0755	TD/Halo	5.8 ± 0.3	$8.8^{+0.2}_{-0.1}$	$0.81^{+0.12}_{-0.1}$	0.2 ± 0.03	$5.9^{+0.9}_{-0.8}$	-162296^{+544}_{-568}	1680^{+41}_{-42}
J1416+1348 B	D	$8.087^{+0.014}_{-0.009}$	$9.72^{+0.05}_{-0.06}$	$0.77^{+0.09}_{-0.13}$	$0.092^{+0.003}_{-0.004}$	$4.7^{+0.5}_{-0.8}$	-151948^{+184}_{-175}	$2113.0^{+1.1}_{-0.9}$
J1416+1348 A	D	$8.096^{+0.012}_{-0.01}$	$9.69^{+0.04}_{-0.06}$	$0.7^{+0.09}_{-0.13}$	$0.089^{+0.003}_{-0.004}$	$4.3^{+0.5}_{-0.7}$	-152055^{+136}_{-131}	$2113.7^{+0.9}_{-0.8}$
HD 126053 B	D	$7.39^{+0.07}_{-0.1}$	$8.96^{+0.04}_{-0.02}$	$0.67^{+0.07}_{-0.1}$	$0.096^{+0.009}_{-0.006}$	$4.5^{+0.5}_{-0.7}$	-156470^{+198}_{-208}	1947^{+4}_{-5}
HIP 70849 B	D	$8.06^{+0.04}_{-0.19}$	$8.35^{+0.13}_{-0.05}$	$0.17^{+0.01}_{-0.02}$	$0.02^{+0.01}_{-0.003}$	$1.2^{+0.09}_{-0.13}$	-156667^{+917}_{-559}	1978^{+31}_{-20}
GJ 576 B	TD	$4.704^{+0.003}_{-0.002}$	$8.52^{+0.04}_{-0.06}$	$1.16^{+0.1}_{-0.14}$	$0.289^{+0.002}_{-0.003}$	$9.3^{+0.7}_{-1.1}$	-167227^{+346}_{-306}	1448 ± 2
Gl 584 C	D	$7.688^{+0.008}_{-0.011}$	$8.9^{+0.2}_{-0.1}$	$0.15^{+0.04}_{-0.07}$	$0.075^{+0.009}_{-0.006}$	$1.0^{+0.3}_{-0.5}$	-155837^{+539}_{-390}	1999^{+18}_{-14}
J1541−2250	D	$7.44^{+0.07}_{-0.05}$	$9.1^{+0.1}_{-0.2}$	$0.07^{+0.03}_{-0.02}$	$0.099^{+0.01}_{-0.016}$	0.5 ± 0.2	-156185^{+396}_{-406}	1980^{+9}_{-10}
J1553+6933	Halo	$0.4^{+0.3}_{-0.1}$	17^{+3}_{-2}	$1.4^{+4.2}_{-1.0}$	$0.957^{+0.009}_{-0.018}$	26^{+36}_{-19}	-147378^{+11762}_{-8556}	-132^{+142}_{-135}
J1626+3925	Halo	$0.53^{+0.06}_{-0.05}$	$10.44^{+0.08}_{-0.06}$	$1.2^{+3.1}_{-0.3}$	$0.904^{+0.008}_{-0.009}$	29^{+11}_{-4}	-170291^{+487}_{-477}	-196^{+28}_{-27}
J1810−1010	D/TD	5.3 ± 0.1	$8.84^{+0.08}_{-0.09}$	$0.64^{+0.05}_{-0.06}$	$0.26^{+0.01}_{-0.02}$	$4.9^{+0.4}_{-0.5}$	-164119^{+307}_{-274}	1601^{+16}_{-22}
J1828+2650	D	$7.95^{+0.07}_{-0.06}$	9.5 ± 0.2	$0.79^{+0.04}_{-0.03}$	$0.088^{+0.009}_{-0.005}$	5.0 ± 0.3	-153187^{+1012}_{-788}	2065^{+39}_{-30}
Wolf 1130 C	TD	$5.0^{+0.2}_{-0.1}$	$11.0^{+0.2}_{-0.1}$	$0.98^{+0.05}_{-0.03}$	$0.375^{+0.005}_{-0.007}$	$6.32^{+0.09}_{-0.05}$	-156603^{+920}_{-1221}	1683^{+36}_{-48}
J2030+0749	D	$7.3^{+0.3}_{-0.2}$	$8.385^{+0.008}_{-0.004}$	$0.15^{+0.03}_{-0.02}$	$0.07^{+0.01}_{-0.02}$	$1.1^{+0.2}_{-0.1}$	-158741^{+831}_{-859}	1899^{+31}_{-33}
HN Peg B	D	$7.4^{+0.3}_{-0.2}$	$8.123^{+0.004}_{-0.005}$	$0.03^{+0.03}_{-0.01}$	$0.05^{+0.01}_{-0.02}$	$0.19^{+0.2}_{-0.08}$	-159669^{+1001}_{-1042}	1874^{+36}_{-39}
Additional Literature: Metal-poor Brown Dwarf								
J1534−1043	Halo	$1.5^{+0.4}_{-0.5}$	$8.8^{+0.2}_{-0.1}$	$5.9^{+0.6}_{-1.1}$	$0.71^{+0.08}_{-0.06}$	57^{+10}_{-8}	-174846^{+1005}_{-897}	495^{+129}_{-118}

Note.
[a] Galactic kinematic populations, including thin disk (D), thick disk (TD), and halo (H). See Section 4.1 for the full definition.

−1043, on the other hand, are consistent with the Milky Way's in situ halo population. Except for J1534−1043, the remaining three sources are notable for exhibiting retrograde Galactic orbits ($L_z < 0$).

The T subdwarfs J0414−5854 (thick disk/halo) and J1316+0755 (thick disk/halo) warrant special attention. As discussed in Section 4, both overlapped with Helmi stream members in the U–V plane and Toomre plot, but not in the U–W plane and V–W plane. Figure 5 shows that they are also highly inconsistent with the Helmi stream in the $E_{\rm tot}$–L_z plane. Instead, both objects reside within the broader thick disk population. Lacking a robust parallax measurement, our kinematic population assignments are preliminary for these two sources.

Verifying the true population membership of these sources will require characterization of their chemical abundances, analysis which will be presented in future studies (see A. M. Meisner et al. 2026 for J1553+6933). Nevertheless, our analysis demonstrates the necessity of considering multiple kinematic diagnostics, in addition to chemical abundances, for determining the Galactic population memberships of nearby sources when comparing to more distributed stellar samples.

5. Individual Objects of Interest

In this section, we discuss objects that exhibit thick disk or halo kinematics and summarize their relevant literature together with our findings in this work, including J0414−5854, J0532+8246, J0645−6646, J1316+0755, J1553+6933, J1626+3925, J1810−1010, and Wolf 1130 C. Here, we only focus on the fundamental and kinematic properties of metal-poor brown dwarfs in our sample. Some of the parameters quoted in this section may change significantly in the upcoming years, as the metal-poor self-consistent models are relatively new owing to their exotic chemistry and rapidly updated opacities. For observed properties such as color, spectral features, and classifications, we refer readers to A. J. Burgasser et al. (2025a) and other earlier works (e.g., N. Lodieu et al. 2015; Z. H. Zhang et al. 2017, 2019; N. Lodieu et al. 2019; A. M. Meisner et al. 2020, 2021; A. C. Schneider et al. 2020, and references in Tables 1 and 2).

J0414−5854. WISE J041451.64−585457.0 was discovered in A. C. Schneider et al. (2020) as one of the prototype T-type extreme subdwarfs. It is an extreme subdwarf (esd) T6 with $T_{\rm eff} = 699^{+66}_{-49}$ K and [M/H] $= -1.34^{+0.17}_{-0.15}$ dex in A. J. Burgasser et al. (2025a). Using our updated proper motions and RV, it is a transitional thick disk/halo member. From our kinematic analysis, it exhibits a moderate Galactic eccentricity of $0.34^{+0.01}_{-0.02}$ and inclination of $17.0^{+1.6}_{-0.5}$ deg, most likely to be a thick disk member and not associated with the Helmi Stream. However, the membership of this first T extreme subdwarf should be revisited once its parallax is available.

J0532+8246. 2MASS J053253.46+824646.5 is an extreme L subdwarf, with a spectral type of esdL7 (A. J. Burgasser et al. 2003; J. D. Kirkpatrick et al. 2010; Z. H. Zhang et al. 2017). It is a well-characterized metal-poor late-L-type brown dwarf (J. D. Kirkpatrick 2005; A. J. Burgasser et al. 2007). While J0532+8246 is substellar, its optical spectra lack

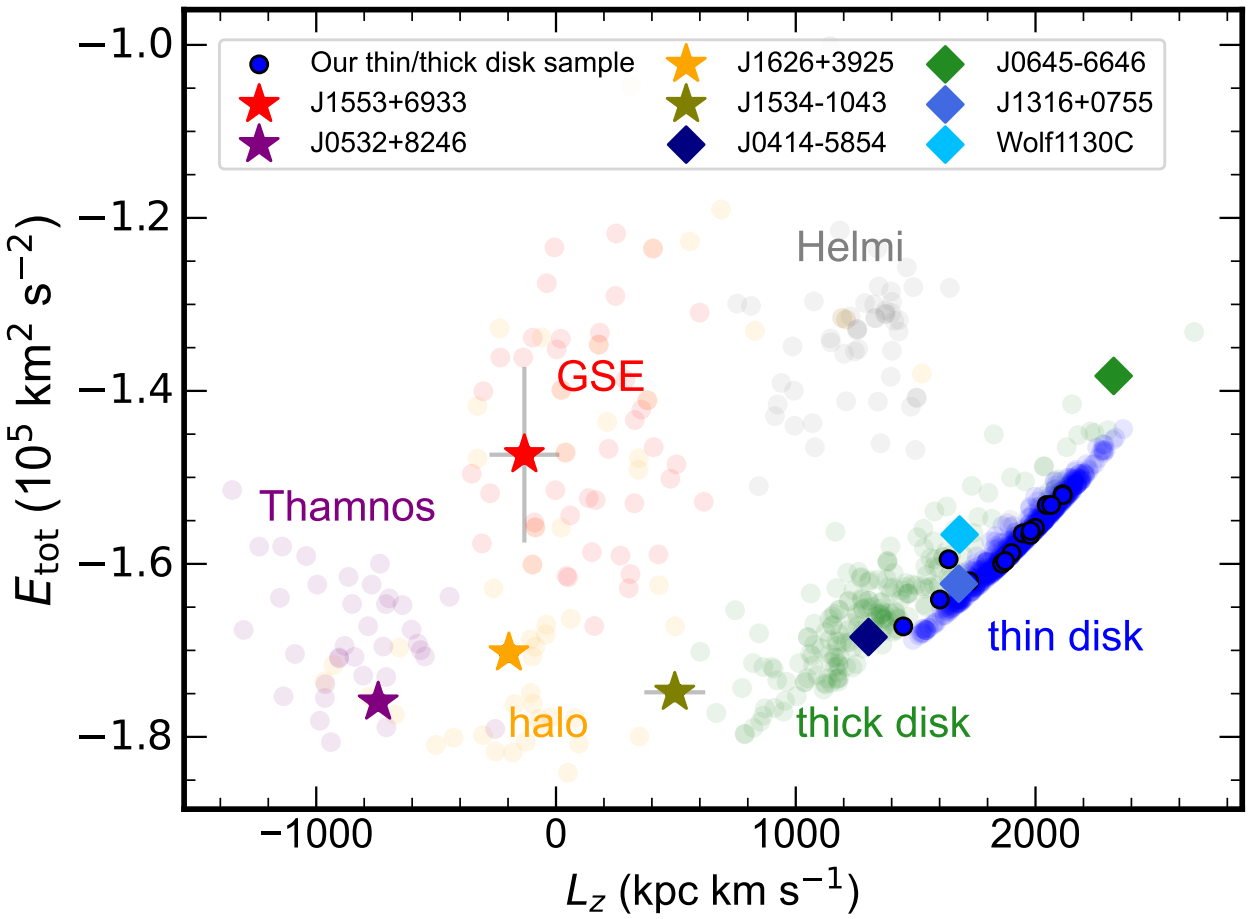


Figure 5. Galactic total energy ($E_{\rm tot}$) versus vertical angular momentum (L_z) for our sample, based on `galpy` (J. Bovy 2015) and the `McMillan17` Galactic potential (P. J. McMillan 2017). Symbols and colors are the same as in Figure 4.

Lithium (N. Lodieu et al. 2015), a species expected for objects of masses below 0.060 $M_\odot$ (I. Baraffe et al. 2003). It has a [Fe/H] ~-1.6 dex and $T_{\rm eff}$ of 1550 ± 175 K (A. J. Burgasser et al. 2025a), and shows halo kinematics and a retrograde Galactic eccentric orbit (A. J. Burgasser et al. 2008), and is consistent with the Thamnos Stream based on the *U*–*V* space and Toomre analysis (A. J. Burgasser et al. 2025a). Based on our RV measurement and kinematic analysis, we confirm that it is a likely member of Thamnos based on our full analysis of *UVW* motions and its $E_{\rm tot}$–L_z. We updated the Galactic orbits of $e = 0.59 \pm 0.02$ and constrained its high inclination of $i = 19^{+1}_{-2}$ deg.

J0645−6646. 2MASS J06453153−6646120 was discovered (J. D. Kirkpatrick et al. 2010) and reclassified as d/sdT0 (A. J. Burgasser et al. 2025a). Its optical spectra lack Lithium (N. Lodieu et al. 2015), with its $T_{\rm eff} = 1419 \pm 81$ K and [M/H] ~-0.4 to $+0.8$ dex (A. J. Burgasser et al. 2025a). We present its RV measurement (consistent with RV $= -33 \pm 10$ km s^{-1} using the VLT X-shooter spectra from Z. H. Zhang et al. 2018), with clear thick disk kinematics. Interestingly, its eccentric ($e = 0.41 \pm 0.02$) Galactic orbit is highly prograde and slightly deviates from the bulk thick disk population, and its maximum Galactic radius of $15.9^{+0.8}_{-0.6}$ kpc is significantly larger than the majority of our sample, other than J1553+6933. It was flagged as a potential binary but with low probability (H. Brooks et al. 2023). While we observed slight mismatches in the spectral fit in 4.66–4.72 μm, the mismatch is not significant enough to support the hypothesis that it is a binary compared to known short-period double-line ultracool dwarf binaries (C.-C. Hsu et al. 2023).

J1316+0755. J131609.68+075553.9 is an sdT6.5 dwarf discovered by B. Burningham et al. (2014). J1316+0755 has a $T_{\rm eff}$ of 765^{+55}_{-50} K and [M/H] $= -0.65^{+0.11}_{-0.09}$ dex (A. J. Burgasser et al. 2025a). It also has a moderately eccentric and inclined Galactic orbit ($e = 0.20 \pm 0.03$ and $i = 5.9^{+0.9}_{-0.8}$ deg. Our kinematic analysis indicates that it is a transitional thick disk and halo object. The evidence of halo membership is based on its *UVW* and Toomre positions and T. Bensby et al. (2003) metrics (Figure 4), while our analysis of $E_{\rm tot}$–L_z places it confidently as a thick disk member (Figure 5). Similar to our discussion of J0414−5854, we rule J1316+0755 out as a member of the Helmi Stream. However, its kinematics should be revisited once its parallax is available.

J1553+6933. This brown dwarf was discovered in A. M. Meisner et al. (2020) as an sdT4 dwarf with metallicity ~-0.5 dex. Recent follow-up analysis indicates that J1553+6933 has $T_{\rm eff} = 1225^{+70}_{-75}$ K and [M/H] $= -1.0^{+0.2}_{-0.3}$ dex, and previously it was proposed as a member of the Helmi Stream (A. J. Burgasser et al. 2025a). Using our updated RV, J1553+6933 is a confirmed halo object associated with Gaia-Enceladus. A. M. Meisner et al. (2026) found that J1553+6933 has effective temperature $T_{\rm eff} = 686$–990 K, metallicity [M/H] $= -1.25^{+0.14}_{-0.21}$ dex, and α-enrichment [α/Fe] $= +0.16^{+0.03}_{-0.04}$ dex. We further verified that all kinematic properties are consistent with the properties defined in the sample curated in H. Ernandes et al. (2024). Our kinematic analyses

based on $E_{\rm tot}$–L_z and Galactic orbital eccentricity ($e = 0.957^{+0.009}_{-0.018}$) make its kinematic association with Gaia-Enceladus highly confident. Its Galactic high orbital inclination ($i = 26^{+36}_{-19}$ deg), small inner Galactic radius ($0.4^{+0.3}_{-0.1}$ kpc), and retrograde Galactic motion are reminiscent of its halo kinematics. It is noted that J1553+6933 does not exhibit any evidence of being a close binary.

J1626+3925. 2MASS J16262034+3925190 was discovered as one of the first L-type subdwarfs and pointed out as a halo object (A. J. Burgasser 2004), and classified as esdL4 (J. E. Gizis & J. Harvin 2006; A. J. Burgasser et al. 2007; Z. H. Zhang et al. 2013, 2017). It is likely a metal-poor low-mass star (A. J. Burgasser 2004; E. Schilbach et al. 2009), consistent with the nondetection of lithium (N. Lodieu et al. 2015). It has $T_{\rm eff}$ = 2148 ± 14 K and [M/H] ∼−1.5 to −2.0 dex (A. J. Burgasser et al. 2007, 2009; E. C. Gonzales et al. 2018), and it has no known companions (B. Goldman et al. 2008). With our refined RV, all of our kinematic analyses place it as a halo object. Its Galactic orbit is retrograde, highly eccentric ($e = 0.904^{+0.008}_{-0.009}$) and inclined ($i = 29^{+11}_{-4}$ deg).

J1810−1010. WISEA J181006.18−101000.5 was discovered in A. C. Schneider et al. (2020) and classified as esdT3 (A. J. Burgasser et al. 2025a). J1810−1010 is nearby (∼9 pc; N. Lodieu et al. 2022), with $T_{\rm eff} = 835 \pm 58$ K (A. J. Burgasser et al. 2025a) and [Fe/H] = −1.7 ± 0.2 dex (J.-Y. Zhang et al. 2025; N. Lodieu et al. 2022). Its $T_{\rm eff}$ is consistent with the detection of CH_4 (J.-Y. Zhang et al. 2025). Our companion paper (N. Lodieu et al. 2026, submitted) shows that J1810−1010 has a metallicity [M/H] = $-1.40^{+0.18}_{-0.11}$ dex and α-enrichment [α/Fe] = $+0.15^{+0.15}_{-0.03}$ dex. Kinematically, our refined RV indicates that J1810−1010 is a transitional thin/thick disk object, with a moderately eccentric and inclined Galactic orbit ($e = 0.26^{+0.01}_{-0.02}$, $i = 4.9^{+0.4}_{-0.5}$ deg).

Wolf 1130 C. Wolf 1130 C is known for an outlier with abundant PH_3 absorption (A. J. Burgasser et al. 2025b). Discovered by G. N. Mace et al. (2013), Wolf 1130 C is a tertiary component comoving with a close binary system (i.e., in a triple system). The close binary is composed of sdM1 GJ 781 A (J. E. Gizis 1997) and white dwarf Wolf 1130B in a 0.5 day orbit (G. N. Mace et al. 2018). Wolf 1130 C was originally classified as an sdT8 dwarf (G. N. Mace et al. 2013; S. E. Logsdon et al. 2018). A. J. Burgasser et al. (2025b) reclassified it as (e)sdT6 with a $T_{\rm eff} = 621 \pm 9$ K and [M/H] = −0.68 ± 0.04 dex. Our kinematic analysis and RV place the Wolf 1130 system as a member of the typical thick disk population, with a moderately eccentric and inclined Galactic orbit.

6. Summary

We have presented the first RV survey of brown dwarfs using JWST/NIRSpec G395H spectroscopy. Our main findings are summarized as follows:

1. We have compiled a kinematic sample of 23 brown dwarfs spanning a broad range of temperatures and metallicities observed with JWST NIRSpec. We report new proper motion measurements for two T subdwarfs, J0414−5854 and J1316+0755, based on multiepoch observations from WISE, VHS, NSC DR2, and UKIDSS, and new high-resolution RV measurements of J1416+1348 A from Keck/NIRSPEC spectra.
2. We have introduced a forward-modeling framework for NIRSpec G395H spectra focused on the 4.4–5.0 μm region, sampling the CO fundamental band. We demonstrate a statistical precision of <0.5 km s^{-1} and a systematic accuracy of 5 km s^{-1} (1/20th of a resolution element, or 1/10th of a pixel), the latter based on comparison with previously reported RVs obtained with ground-based high-resolution spectroscopy.
3. Combining astrometry and RVs, we determined *UVW* space motions for our complete sample to median precisions of 3 km s^{-1}. These measurements allow us to associate our targets with various Galactic populations. Half of our sample, primarily benchmark companions to solar/near-solar-metallicity stars, are thin disk objects; J0448−1935 and J1810−1010 are transitional thin/thick disk objects; J0645−6646, GJ 576 B, Wolf 1130 C are thick disk objects; J0414−5854 and J1316+0755are transitional thick disk/halo objects; and J0532+8246, J1553+6933, J1626+3925, and J1534−1043 are all halo objects.
4. We inferred Galactic orbits for our sample, finding a progressive increase in eccentricity and absolute inclination from thin disk to thick disk to halo. Sources in the last two populations naturally divide into radially inbound and passing trajectories. The halo objects J1553+6933 and J1626+3925 have the most eccentric inbound orbits, passing within 1 kpc of the Galactic center at perigalacticon; while outbound subdwarf J0645−6646 and J1553+6933 have orbits that take them to Galactic radii beyond 15 kpc.
5. Analyzing the total orbital energy and angular momentum of our sources, we have confirmed that J1553+6933 is likely to be a member of Gaia-Enceladus, consistent with its elemental abundances, and J0532+8246 is an excellent match to the Thamnos Stream.

This study demonstrates that JWST/NIRSpec G395H spectroscopy provides robust and reliable RVs for cool and faint brown dwarfs sufficient for Galactic kinematic studies. Combined with the ability to infer detailed abundances from these data through retrieval modeling (J. K. Faherty et al. 2024, 2025; M. J. Rowland et al. 2024; A. J. Burgasser et al. 2025b), G395H spectra enable brown dwarfs to be physically characterized in the same precise manner as hotter stars. By combining measurements from the 6D kinematics plus abundances of these local brown dwarfs with the physical properties and spatial distributions of more distant brown dwarfs in the Galactic thick disk and halo (C. Aganze et al. 2022a, 2022b; A. J. Burgasser et al. 2024; K. N. Hainline et al. 2026), globular clusters (R. Gerasimov et al. 2022, 2024a, 2024b), and even the SMC (P. Zeidler et al. 2024), new insights can be gained about the Milky Way's formation history and assembly from its lowest-mass members. When hundreds of brown dwarfs in the Galactic halo and substructures are confirmed, constraints on the substellar mass function and star formation rate across cosmic age and in metal-poor environments will be possible beyond local environments (J. D. Kirkpatrick et al. 2021a, 2024; W. M. J. Best et al. 2024).

Acknowledgments

The authors thank the anonymous referee for the useful suggestions that improved this manuscript. C.C.H., C.A.T.,

A.J.B., E.G., and G.S. acknowledge funding support from NASA/STScI through JWST General Observer Program GO-4668, under NASA contract NAS 5-03127. A.J.B. and E.G. acknowledge funding support from the Heising-Simons Foundation. N.L. acknowledges support from the Agencia Estatal de Investigación del Ministerio de Ciencia e Innovación (AEI-MCINN) under grant PID2022-137241NB-C41. All of the data presented in this paper were obtained from the Mikulski Archive for Space Telescopes (MAST) at the Space Telescope Science Institute. The specific observations analyzed can be accessed via doi:10.17909/zm7x-dx89. STScI is operated by the Association of Universities for Research in Astronomy, Inc., under NASA contract NAS 5-26555. Support to MAST for these data is provided by the NASA Office of Space Science via grant NAG5-7584 and by other grants and contracts.

Facilities: JWST (NIRSpec), Keck:II (NIRSPEC).

Software: `Astropy` (Astropy Collaboration et al. 2013, 2018), `corner` (D. Foreman-Mackey 2016), `emcee` (D. Foreman-Mackey et al. 2013), `galpy` (J. Bovy 2015), `Matplotlib` (J. D. Hunter 2007), `Numpy` (C. R. Harris et al. 2020), `PyAstronomy` (S. Czesla et al. 2019), `Scipy` (P. Virtanen et al. 2020), `SPLAT` (A. J. Burgasser & Splat Development Team 2017), `SMART` (C.-C. Hsu et al. 2021a, 2021b).

Appendix
Best-fit Parameters for Our Sample

In Section 3.1, we show our forward-model method. Here we provide the Sonora Elf-Owl best-fit substellar atmosphere model parameters in Table A1 for interested readers to reproduce our results. Other than RV, our best-fit parameters listed here should not be used as accurate determinations, as several studies in the literature have shown that focusing on a relatively narrow wavelength range could bias the true parameters of ultracool dwarfs (e.g., C.-C. Hsu et al. 2021b, 2024a, 2024b), and our forward-model includes a second-order polynomial continuum correction, which would bias the inferred $T_{\rm eff}$ and other parameters. As for $v \sin i$, the resolution of our G395H spectra is ∼3300 at 4.4–5.0 μm, which corresponds to a $v \sin i$ floor ∼90.8 km s^{-1}. Most brown dwarfs have $v \sin i$<90 km s^{-1} (C.-C. Hsu et al. 2021b; M. E. Tannock et al. 2021; C.-C. Hsu et al. 2024a, 2026), and G395H resolution is insufficient to provide robust $v \sin i$ (for example, discrepant $v \sin i$ of J1828+2650 was reported using G395H spectra in B. W. P. Lew et al. 2024).

Table A1
Sonora Elf-Owl Best-fit Parameters for Our Sample

Name	$T_{\rm eff}$ (K)	$\log g$ (cm s^{-2})	[M/H] (dex)	C/O[a]	$\log K_{zz}$ (cm^2 s^{-1})	$v \sin i$ (km s^{-1})	RV (km s^{-1})
J0414−5854	818^{+4}_{-5}	$5.253^{+0.012}_{-0.009}$	$-0.995^{+0.006}_{-0.003}$	$0.24^{+0.02}_{-0.01}$	$5.4^{+0.2}_{-0.4}$	27^{+22}_{-17}	$130.3^{+0.4}_{-0.5}$
J0415−0935	699^{+2}_{-4}	3.92 ± 0.04	−0.84 ± 0.02	$0.39^{+0.02}_{-0.03}$	$7.12^{+0.16}_{-0.09}$	16^{+9}_{-10}	46.8 ± 0.2
J0448−1935	922 ± 5	$4.55^{+0.04}_{-0.03}$	$-0.997^{+0.006}_{-0.002}$	$0.2303^{+0.0026}_{-0.001}$	6.93 ± 0.01	53^{+5}_{-8}	92.0 ± 0.3
J0532+8246	1789 ± 6	$5.496^{+0.003}_{-0.007}$	$-0.994^{+0.009}_{-0.004}$	$0.239^{+0.011}_{-0.008}$	$7.7^{+0.1}_{-0.3}$	44^{+3}_{-6}	−173.4 ± 0.2
J0645−6646	1672 ± 11	$5.49^{+0.01}_{-0.02}$	−0.36 ± 0.04	0.382 ± 0.007	$7.8^{+0.1}_{-0.3}$	55^{+5}_{-9}	−25.4 ± 0.3
HIP 38939 B	1233^{+10}_{-9}	$5.03^{+0.07}_{-0.1}$	$-0.55^{+0.03}_{-0.04}$	0.28 ± 0.02	$7.2^{+0.3}_{-0.2}$	17^{+12}_{-11}	−14.0 ± 0.2
J0836−1859	600^{+10}_{-9}	$3.6^{+0.06}_{-0.07}$	$-0.988^{+0.016}_{-0.009}$	0.29 ± 0.03	7.2 ± 0.2	24^{+14}_{-15}	$21.6^{+0.5}_{-0.6}$
J1316+0755	606^{+5}_{-4}	$4.1^{+0.05}_{-0.04}$	−0.96 ± 0.02	$0.232^{+0.004}_{-0.002}$	$6.95^{+0.01}_{-0.02}$	59^{+4}_{-9}	24.8 ± 0.4
J1416+1348 B	638 ± 2	4.61 ± 0.02	−0.691 ± 0.005	$0.2301^{+0.0016}_{-0.0008}$	4.4 ± 0.3	24^{+6}_{-12}	−51.5 ± 0.2
J1416+1348 A	1900 ± 7	$5.44^{+0.03}_{-0.04}$	−0.65 ± 0.03	$0.457^{+0.007}_{-0.005}$	$7.97^{+0.03}_{-0.06}$	24^{+14}_{-15}	−48.2 ± 0.2
HD 126053 B	545^{+6}_{-9}	3.9 ± 0.04	$-0.989^{+0.01}_{-0.008}$	$0.231^{+0.003}_{-0.002}$	6.924 ± 0.008	29^{+7}_{-15}	−24.8 ± 0.3
HIP 70849 B	1342 ± 5	$5.49^{+0.007}_{-0.016}$	$0.612^{+0.01}_{-0.011}$	0.419 ± 0.005	$5.4^{+0.4}_{-0.5}$	25^{+9}_{-13}	−4.9 ± 0.2
GJ 576 B	978 ± 5	5.0 ± 0.01	$-0.494^{+0.011}_{-0.005}$	$0.32^{+0.01}_{-0.02}$	$5.6^{+0.4}_{-0.6}$	33^{+7}_{-14}	−89.8 ± 0.2
Gl 584 C	1677 ± 7	$5.48^{+0.02}_{-0.03}$	0.23 ± 0.02	0.618 ± 0.007	7.2 ± 0.2	9^{+9}_{-6}	−13.8 ± 0.2
J1534−1043	832^{+25}_{-32}	$5.486^{+0.01}_{-0.021}$	$-0.98^{+0.02}_{-0.01}$	$0.6^{+0.4}_{-0.2}$	$6.9^{+0.6}_{-0.2}$	195^{+3}_{-6}	−130 ± 5
J1541−2250	475^{+4}_{-3}	$3.52^{+0.05}_{-0.03}$	$-0.997^{+0.005}_{-0.002}$	$0.55^{+0.07}_{-0.09}$	$7.91^{+0.06}_{-0.09}$	10^{+9}_{-8}	−38.7 ± 0.4
J1553+6933	1011 ± 5	5.11 ± 0.02	$-0.996^{+0.007}_{-0.003}$	$0.233^{+0.006}_{-0.003}$	6.91 ± 0.01	48^{+9}_{-18}	−162.7 ± 0.4
J1626+3925	2398^{+1}_{-3}	$3.57^{+0.06}_{-0.08}$	$-0.99^{+0.02}_{-0.01}$	$0.56^{+0.02}_{-0.03}$	$7.7^{+0.2}_{-0.4}$	48^{+14}_{-21}	$-256.6^{+0.9}_{-1.0}$
J1810−1010	1137^{+11}_{-18}	$5.497^{+0.002}_{-0.012}$	$-0.998^{+0.006}_{-0.002}$	$0.237^{+0.036}_{-0.006}$	$5.0^{+0.5}_{-1.0}$	119^{+43}_{-20}	$-85.2^{+0.9}_{-1.1}$
J1828+2650	400.0 ± 0.3	$4.252^{+0.013}_{-0.009}$	−0.634 ± 0.007	$0.2297^{+0.0011}_{-0.0005}$	6.972 ± 0.008	3^{+4}_{-2}	−30.9 ± 0.2
Wolf 1130 C	665^{+5}_{-8}	$4.98^{+0.02}_{-0.07}$	$-0.82^{+0.01}_{-0.03}$	$0.236^{+0.01}_{-0.006}$	$5.7^{+0.2}_{-0.3}$	16^{+16}_{-11}	−37.8 ± 0.3
J2030+0749	1494^{+6}_{-7}	$5.492^{+0.006}_{-0.013}$	0.34 ± 0.01	$0.69^{+0.006}_{-0.003}$	$6.52^{+0.08}_{-0.11}$	19^{+8}_{-11}	−28.3 ± 0.1
HN Peg B	1365^{+24}_{-21}	$5.48^{+0.01}_{-0.03}$	0.61 ± 0.03	0.492 ± 0.009	$6.5^{+0.2}_{-0.5}$	22^{+7}_{-14}	−19.8 ± 0.2

Note.
[a] The solar elemental abundance C/O = 0.458.

ORCID iDs

Chih-Chun Hsu https://orcid.org/0000-0002-5370-7494
Christopher A. Theissen https://orcid.org/0000-0002-9807-5435
Adam J. Burgasser https://orcid.org/0000-0002-6523-9536
Adam C. Schneider https://orcid.org/0000-0002-6294-5937
Christian Aganze https://orcid.org/0000-0003-2094-9128
Aaron M. Meisner https://orcid.org/0000-0002-1125-7384
Jonathan Gagné https://orcid.org/0000-0002-2592-9612
Nicolas Lodieu https://orcid.org/0000-0002-3612-8968
ZengHua Zhang https://orcid.org/0000-0003-3047-607X
Genaro Suárez https://orcid.org/0000-0002-2011-4924
Eileen C. Gonzales https://orcid.org/0000-0003-4636-6676
Jacqueline K. Faherty https://orcid.org/0000-0001-6251-0573
Jason J. Wang (王劲飞) https://orcid.org/0000-0003-0774-6502
Stanimir A. Metchev https://orcid.org/0000-0003-3050-8203
Dan Caselden https://orcid.org/0000-0001-7896-5791
Michael C. Cushing https://orcid.org/0000-0001-7780-3352
Roman Gerasimov https://orcid.org/0000-0003-0398-639X

References

Abazajian, K. N., Adelman-McCarthy, J. K., Agüeros, M. A., et al. 2009, ApJS, 182, 543
Aganze, C., Burgasser, A. J., Malkan, M., et al. 2022a, ApJ, 924, 114
Aganze, C., Burgasser, A. J., Malkan, M., et al. 2022b, ApJ, 934, 73
Alejandro Merchan, S., Faherty, J. K., Suárez, G., et al. 2025, ApJ, 989, 80
Allard, F., Homeier, D., & Freytag, B. 2012, RSPTA, 370, 2765
Alvarado, E., Gerasimov, R., Burgasser, A. J., et al. 2024, RNAAS, 8, 134
Astropy Collaboration, Price-Whelan, A. M., Sipőcz, B. M., et al. 2018, AJ, 156, 123
Astropy Collaboration, Robitaille, T. P., Tollerud, E. J., et al. 2013, A&A, 558, A33
Aumer, M., & Binney, J. J. 2009, MNRAS, 397, 1286
Baraffe, I., Chabrier, G., Barman, T. S., Allard, F., & Hauschildt, P. H. 2003, A&A, 402, 701
Belokurov, V. 2013, NewAR, 57, 100
Belokurov, V., Erkal, D., Evans, N. W., Koposov, S. E., & Deason, A. J. 2018, MNRAS, 478, 611
Bensby, T., Feltzing, S., & Lundström, I. 2003, A&A, 410, 527
Best, W. M. J., Sanghi, A., Liu, M. C., Magnier, E. A., & Dupuy, T. J. 2024, ApJ, 967, 115
Best, W. M. J., Liu, M. C., Magnier, E. A., et al. 2013, ApJ, 777, 84
Blake, C. H., Charbonneau, D., & White, R. J. 2010, ApJ, 723, 684
Blake, C. H., Charbonneau, D., White, R. J., Marley, M. S., & Saumon, D. 2007, ApJ, 666, 1198
Bland-Hawthorn, J., & Gerhard, O. 2016, ARA&A, 54, 529
Bonaca, A., & Price-Whelan, A. M. 2025, NewAR, 100, 101713
Bovy, J. 2015, ApJS, 216, 29
Brooks, H., Kirkpatrick, J. D., Meisner, A. M., et al. 2023, AJ, 165, 232
Burgasser, A. J. 2004, ApJL, 614, L73
Burgasser, A. J., Bezanson, R., Labbe, I., et al. 2024, ApJ, 962, 177
Burgasser, A. J., Blake, C. H., Gelino, C. R., Sahlmann, J., & Bardalez Gagliuffi, D. 2016, ApJ, 827, 25
Burgasser, A. J., Cruz, K. L., & Kirkpatrick, J. D. 2007, ApJ, 657, 494
Burgasser, A. J., Geballe, T. R., Leggett, S. K., Kirkpatrick, J. D., & Golimowski, D. A. 2006, ApJ, 637, 1067
Burgasser, A. J., Gonzales, E. C., Beiler, S. A., et al. 2025b, Sci, 390, 697
Burgasser, A. J., Kirkpatrick, J. D., Brown, M. E., et al. 2002, ApJ, 564, 421
Burgasser, A. J., Kirkpatrick, J. D., Burrows, A., et al. 2003, ApJ, 592, 1186
Burgasser, A. J., Logsdon, S. E., Gagné, J., et al. 2015b, ApJS, 220, 18
Burgasser, A. J., Melis, C., Todd, J., et al. 2015a, AJ, 150, 180
Burgasser, A. J., Schneider, A. C., Meisner, A. M., et al. 2025a, ApJ, 982, 79
Burgasser, A. J. & Splat Development Team 2017, ASInC, 14, 7
Burgasser, A. J., Vrba, F. J., Lépine, S., et al. 2008, ApJ, 672, 1159
Burgasser, A. J., Witte, S., Helling, C., et al. 2009, ApJ, 697, 148
Burningham, B., Leggett, S. K., Lucas, P. W., et al. 2010, MNRAS, 404, 1952
Burningham, B., Smith, L., Cardoso, C. V., et al. 2014, MNRAS, 440, 359
Burrows, A., Hubbard, W. B., Lunine, J. I., & Liebert, J. 2001, RvMP, 73, 719
Bushouse, H., Eisenhamer, J., Dencheva, N., et al. 2026, JWST Calibration Pipeline, v2.0.1, Zenodo, doi: 10.5281/zenodo.20058613
Carvalho, A., & Johns-Krull, C. M. 2023, RNAAS, 7, 91
Chakrabarti, S., Stevens, D. J., Wright, J., et al. 2022, ApJL, 928, L17
Chen, A. Y. A., Goto, T., Wu, C. K.-W., et al. 2025, PASA, 42, e042
Conroy, C., Bonaca, A., Cargile, P., et al. 2019, ApJ, 883, 107
Cooper, A. P., Koposov, S. E., Allende Prieto, C., et al. 2023, ApJ, 947, 37
Cushing, M. C., Kirkpatrick, J. D., Gelino, C. R., et al. 2011, ApJ, 743, 50
Cushing, M. C., Looper, D., Burgasser, A. J., et al. 2009, ApJ, 696, 986
Cutri, R. M., Wright, E. L., Conrow, T., et al. 2014, yCat, 2328, 0
Czesla, S., Schröter, S., Schneider, C. P., et al. 2019, PyA: Python astronomy-related packages, Astrophysics Source Code Library, ascl: 1906.010
Day-Jones, A. C., Marocco, F., Pinfield, D. J., et al. 2013, MNRAS, 430, 1171
De Silva, G. M., Freeman, K. C., Bland-Hawthorn, J., et al. 2015, MNRAS, 449, 2604
Deason, A. J., & Belokurov, V. 2024, NewAR, 99, 101706
Del Burgo, C., Martín, E. L., Zapatero Osorio, M. R., & Hauschildt, P. H. 2009, A&A, 501, 1059
Di Matteo, P., Haywood, M., Lehnert, M. D., et al. 2019, A&A, 632, A4
Dieterich, S. B., Henry, T. J., Jao, W.-C., et al. 2014, AJ, 147, 94
Duong, L., Freeman, K. C., Asplund, M., et al. 2018, MNRAS, 476, 5216
Dupuy, T. J., & Liu, M. C. 2012, ApJS, 201, 19
Dupuy, T. J., & Liu, M. C. 2017, ApJS, 231, 15
Eisenhardt, P. R. M., Marocco, F., Fowler, J. W., et al. 2020, ApJS, 247, 69
Ernandes, H., Feuillet, D., Feltzing, S., & Skúladóttir, Á. 2024, A&A, 691, A333
Faherty, J. K., Burgasser, A. J., Cruz, K. L., et al. 2009, AJ, 137, 1
Faherty, J. K., Burningham, B., Gagné, J., et al. 2024, Natur, 628, 511
Faherty, J. K., Meisner, A. M., Burningham, B., et al. 2025, Natur, 645, 62
Filippazzo, J. C., Rice, E. L., Faherty, J., et al. 2015, ApJ, 810, 158
Foreman-Mackey, D. 2016, JOSS, 1, 24
Foreman-Mackey, D., Hogg, D. W., Lang, D., & Goodman, J. 2013, PASP, 125, 306
Gaia Collaboration, Prusti, T., de Bruijne, J. H. J., et al. 2016, A&A, 595, A1
Gaia Collaboration, Smart, R. L., Sarro, L. M., et al. 2021, A&A, 649, A6
Gaia Collaboration, Vallenari, A., Brown, A. G. A., et al. 2023, A&A, 674, A1
Gallart, C., Bernard, E. J., Brook, C. B., et al. 2019, NatAs, 3, 932
Gerasimov, R., Bedin, L. R., Burgasser, A. J., et al. 2024a, ApJ, 971, 65
Gerasimov, R., Burgasser, A. J., Caiazzo, I., et al. 2024b, ApJ, 961, 139
Gerasimov, R., Burgasser, A. J., Homeier, D., et al. 2022, ApJ, 930, 24
Gizis, J. E. 1997, AJ, 113, 806
Gizis, J. E., & Harvin, J. 2006, AJ, 132, 2372
Glidic, K., Keyes, T., Zeidler, P., et al. 2025, Tech. Rep. JWST-STScI-009239, STScI
Goldman, B., Bouy, H., Zapatero Osorio, M. R., et al. 2008, A&A, 490, 763
Gonzales, E. C., Faherty, J. K., Gagné, J., Artigau, É., & Bardalez Gagliuffi, D. 2018, ApJ, 864, 100
Gully-Santiago, M. A., Herczeg, G. J., Czekala, I., et al. 2017, ApJ, 836, 200
Hainline, K. N., Helton, J. M., Johnson, B. D., et al. 2024, ApJ, 964, 66
Hainline, K. N., Helton, J. M., Miles, B. E., et al. 2026, ApJ, 1004, 223
Halbwachs, J.-L., Mayor, M., & Udry, S. 2018, A&A, 619, A81
Harris, C. R., Millman, K. J., van der Walt, S. J., et al. 2020, Natur, 585, 357
Hayashi, C., & Nakano, T. 1963, PThPh, 30, 460
Helmi, A. 2008, A&ARv, 15, 145
Helmi, A. 2020, ARA&A, 58, 205
Helmi, A., Babusiaux, C., Koppelman, H. H., et al. 2018, Natur, 563, 85
Holwerda, B. W., Hsu, C.-C., Hathi, N., et al. 2024, MNRAS, 529, 1067
Holwerda, B. W., Trenti, M., Clarkson, W., et al. 2014, ApJ, 788, 77
Hsu, C.-C., Burgasser, A. J., & Theissen, C. A. 2023, ApJL, 945, L6
Hsu, C.-C., Theissen, C., Burgasser, A., & Birky, J. 2021a, SMART: The Spectral Modeling Analysis and RV Tool, v1.0.0, Zenodo, doi: 10.5281/zenodo.4765258
Hsu, C.-C., Burgasser, A. J., Theissen, C. A., et al. 2021b, ApJS, 257, 45
Hsu, C.-C., Burgasser, A. J., Theissen, C. A., et al. 2024a, ApJS, 274, 40
Hsu, C.-C., Wang, J. J., Xuan, J. W., et al. 2024b, ApJ, 971, 9
Hsu, C.-C., Wang, J. J., Xuan, J. W., et al. 2026, AJ, 171, 224
Hunter, J. D. 2007, CSE, 9, 90
Ivezić, Ž., Beers, T. C., & Jurić, M. 2012, ARA&A, 50, 251
Jakobsen, P., Ferruit, P., Alves de Oliveira, C., et al. 2022, A&A, 661, A80
Johnson, D. R. H., & Soderblom, D. R. 1987, AJ, 93, 864
Jurić, M., Ivezić, Ž., Brooks, A., et al. 2008, ApJ, 673, 864
Karpov, S., Malkov, O., & Avdeeva, A. 2025, A&A, 695, A195

Kirkpatrick, J. D. 2005, ARA&A, 43, 195
Kirkpatrick, J. D., Cushing, M. C., Gelino, C. R., et al. 2011, ApJS, 197, 19
Kirkpatrick, J. D., Gelino, C. R., Faherty, J. K., et al. 2021a, ApJS, 253, 7
Kirkpatrick, J. D., Looper, D. L., Burgasser, A. J., et al. 2010, ApJS, 190, 100
Kirkpatrick, J. D., Marocco, F., Caselden, D., et al. 2021b, ApJL, 915, L6
Kirkpatrick, J. D., Marocco, F., Gelino, C. R., et al. 2024, ApJS, 271, 55
Kirkpatrick, J. D., Reid, I. N., Liebert, J., et al. 2000, AJ, 120, 447
Koppelman, H. H., Helmi, A., Massari, D., Roelenga, S., & Bastian, U. 2019, A&A, 625, A5
Kumar, S. S. 1962, AJ, 67, 579
Kumar, S. S. 1963, ApJ, 137, 1121
Lawrence, A., Warren, S. J., Almaini, O., et al. 2007, MNRAS, 379, 1599
Lew, B. W. P., Roellig, T., Batalha, N. E., et al. 2024, AJ, 167, 237
Li, D. H., Zhang, Z. H., Peng, H. H., et al. 2026, MNRAS, 547, stag227
Limbach, M. A., Vos, J. M., Winn, J. N., et al. 2021, ApJ, 918, L25
Lodders, K., Palme, H., & Gail, H.-P. 2009, LanB, 4B, 712
Lodieu, N., Allard, F., Rodrigo, C., et al. 2019, A&A, 628, A61
Lodieu, N., Burgasser, A. J., Pavlenko, Y., & Rebolo, R. 2015, A&A, 579, A58
Lodieu, N., Pérez-Garrido, A., Béjar, V. J. S., et al. 2014, A&A, 569, A120
Lodieu, N., Zapatero Osorio, M. R., Martín, E. L., Rebolo López, R., & Gauza, B. 2022, A&A, 663, A84
Logsdon, S. E., Mace, G. N., McLean, I. S., & Martin, E. C. 2018, ApJ, 867, 96
Luhman, K. L., Patten, B. M., Marengo, M., et al. 2007, ApJ, 654, 570
Mace, G. N., Kirkpatrick, J. D., Cushing, M. C., et al. 2013, ApJ, 777, 36
Mace, G. N., Mann, A. W., Skiff, B. A., et al. 2018, ApJ, 854, 145
Majewski, S. R., Schiavon, R. P., Frinchaboy, P. M., et al. 2017, AJ, 154, 94
Marocco, F., Eisenhardt, P. R. M., Fowler, J. W., et al. 2021, ApJS, 253, 8
Marocco, F., Kirkpatrick, J. D., Schneider, A. C., et al. 2024, ApJ, 967, 147
Marocco, F., Kirkpatrick, J. D., Smart, R. L., et al. 2026, AJ, 171, 284
McLean, I. S., Becklin, E. E., Bendiksen, O., et al. 1998, SPIE, 3354, 566
McLean, I. S., Graham, J. R., Becklin, E. E., et al. 2000, SPIE, 4008, 1048
McMahon, R. G., Banerji, M., Gonzalez, E., et al. 2013, Msngr, 154, 35
McMillan, P. J. 2017, MNRAS, 465, 76
Meisner, A. M., Burgasser, A. J., Hsu, C.-C., et al. 2026, arXiv:2609.29365
Meisner, A. M., Caselden, D., Schlafly, E. F., & Kiwy, F. 2023, AJ, 165, 36
Meisner, A. M., Faherty, J. K., Kirkpatrick, J. D., et al. 2020, ApJ, 899, 123
Meisner, A. M., Schneider, A. C., Burgasser, A. J., et al. 2021, ApJ, 915, 120
Moehler, S., Modigliani, A., Freudling, W., et al. 2014, A&A, 568, A9
Morrissey, S. J., Burgasser, A. J., de Graaff, A., McConachie, I., & Brammer, G. 2026, AJ, 171, 191
Mukherjee, S., Fortney, J. J., Morley, C. V., et al. 2024, ApJ, 963, 73
Myeong, G. C., Evans, N. W., Belokurov, V., Sanders, J. L., & Koposov, S. E. 2018, ApJL, 863, L28
Naidu, R. P., Conroy, C., Bonaca, A., et al. 2020, ApJ, 901, 48
Nakajima, T., Oppenheimer, B. R., Kulkarni, S. R., et al. 1995, Natur, 378, 463
Nidever, D. L., Dey, A., Fasbender, K., et al. 2021, AJ, 161, 192
Nissen, P. E., Amarsi, A. M., Skúladóttir, Á., & Schuster, W. J. 2024, A&A, 682, A116
Nissen, P. E., & Schuster, W. J. 2010, A&A, 511, L10
Nonino, M., Glazebrook, K., Burgasser, A. J., et al. 2023, ApJL, 942, L29
Pinfield, D. J., Burningham, B., Lodieu, N., et al. 2012, MNRAS, 422, 1922
Rebolo, R., Martin, E. L., Basri, G., Marcy, G. W., & Zapatero-Osorio, M. R. 1996, ApJL, 469, L53
Reid, I. N., Kirkpatrick, J. D., Liebert, J., et al. 2002, AJ, 124, 519
Reiners, A., & Basri, G. 2006, AJ, 131, 1806
Rix, H.-W., & Bovy, J. 2013, A&ARv, 21, 61
Rowland, M. J., Morley, C. V., Miles, B. E., et al. 2024, ApJL, 977, L49
Ryan, R. E., Jr., Hathi, N. P., Cohen, S. H., & Windhorst, R. A. 2005, ApJL, 631, L159
Ryan, R. E., Thorman, P. A., Yan, H., et al. 2011, ApJ, 739, 83
Ryan, R. E., Jr., Thorman, P. A., Schmidt, S. J., et al. 2017, ApJ, 847, 53
Schilbach, E., Röser, S., & Scholz, R.-D. 2009, A&A, 493, L27
Schneider, A. C., Burgasser, A. J., Gerasimov, R., et al. 2020, ApJ, 898, 77
Schneider, A. C., Kuchner, M. J., Faherty, J. K., et al. 2026, AJ, 171, 341
Schneider, A. C., Meisner, A. M., Gagné, J., et al. 2021, ApJ, 921, 140
Schneider, A. C., Munn, J. A., Vrba, F. J., et al. 2023, AJ, 166, 103
Schneider, A. C., Vrba, F. J., Bruursema, J., et al. 2025, AJ, 170, 86
Schönrich, R., Binney, J., & Dehnen, W. 2010, MNRAS, 403, 1829
Sivarani, T., Lépine, S., Kembhavi, A. K., & Gupchup, J. 2009, ApJL, 694, L140
Soubiran, C., Jasniewicz, G., Chemin, L., et al. 2018, A&A, 616, A7
Tang, S.-Y., Johns-Krull, C. M., Prato, L., & Stahl, A. G. 2024, ApJ, 973, 124
Tannock, M. E., Metchev, S., Heinze, A., et al. 2021, AJ, 161, 224
Theissen, C. A., Konopacky, Q. M., Lu, J. R., et al. 2022, ApJ, 926, 141
Tran, H. D., Cohen, R., Colson, A., et al. 2016, SPIE, 9910, 99102E
Tu, Z., Wang, S., Chen, X., & Liu, J. 2025a, ApJS, 281, 49
van Leeuwen, F. 2007, A&A, 474, 653
Virtanen, P., Gommers, R., Oliphant, T. E., et al. 2020, NatMet, 17, 261
Vos, J. M., Faherty, J. K., Gagné, J., et al. 2022, ApJ, 924, 68
Whitebook, S., Rodriguez, A. C., Burdge, K., et al. 2026, ApJL, 1000, L23
Wielen, R. 1977, A&A, 60, 263
Xie, R., Yuan, Z., Li, H., et al. 2026, ApJ, 999, 69
Xuan, J. W., Mérand, A., Thompson, W., et al. 2024, Natur, 634, 1070
Zapatero Osorio, M. R., Martín, E. L., Béjar, V. J. S., et al. 2007, ApJ, 666, 1205
Zeidler, P., Sabbi, E., Nota, A., et al. 2024, ApJ, 975, 18
Zhang, J.-Y., Lodieu, N., Martín, E. L., et al. 2025, ApJL, 984, L35
Zhang, J.-Y., Lodieu, N., Martín, E. L., et al. 2025, A&A, 698, A141
Zhang, W., Schneider, A. C., Bickle, T. P., et al. 2025, AJ, 170, 277
Zhang, Z. H., Burgasser, A. J., Gálvez-Ortiz, M. C., et al. 2019, MNRAS, 486, 1260
Zhang, Z. H., Galvez-Ortiz, M. C., Pinfield, D. J., et al. 2018, MNRAS, 480, 5447
Zhang, Z. H., Pinfield, D. J., Burningham, B., et al. 2013, MNRAS, 434, 1005
Zhang, Z. H., Pinfield, D. J., Gálvez-Ortiz, M. C., et al. 2017, MNRAS, 464, 3040